FE-based simulation and validation of a pedestrian impact detection system

Master's thesis in Mobility Engineering

Hanying Zeng

DEPARTMENT OF MECHANICS AND MARITIME SCIENCES

CHALMERS UNIVERSITY OF TECHNOLOGY
Gothenburg, Sweden 2025
www.chalmers.se

Master's Thesis in Mobility Engineering 2025

FE-based simulation and validation of a pedestrian impact detection system

HANYING ZENG

CHALMERS
UNIVERSITY OF TECHNOLOGY

Department of Mechanics and Maritime Sciences
Division of Pedestrian Safety
Chalmers University of Technology
Gothenburg, Sweden 2025

FE-based simulation and validation of a pedestrian impact detection system
HANYING ZENG

© HANYING ZENG, 2025.

Supervisor: Nils Olofsson, Volvo Cars
Examiner:Johan Iraeus, Mechanics and Maritime Sciences

Master's Thesis 2025
Department of Mechanics and Maritime Sciences
Chalmers University of Technology
SE-412 96 Gothenburg
Sweden
Telephone +46 31 772 1000

Typeset in LaTeX
Gothenburg, Sweden 2025

FE-based simulation and validation of a pedestrian impact detection system
HANYING ZENG
Department of Mechanics and Maritime Sciences
Chalmers University of Technology

Abstract

According to the European Commission, pedestrians accounted for 18.4% of road traffic fatalities in the EU in 2023 [5]. Modern vehicles integrate systems such as the Active Hood Lift System (AHLS), which lifts the bonnet to reduce head trauma during pedestrian collisions[3]. A key component enabling AHLS is the pressure-sensitive sensor tube, which detects frontal impacts and triggers hood deployment within milliseconds. To support the deployment of AHLS, this project aimed to develop and validate a Finite Element (FE) model of an air-filled pressure sensor tube for use in pedestrian impact detection. The model was implemented in LS-DYNA and evaluated against physical impact tests conducted at three velocities. Waveform correlation between simulated and measured pressure signals was assessed using the Waveform Index Factor (WIFac) to quantify model accuracy.

The model was assessed under varying configurations to evaluate its predictive accuracy. Foam material properties and fixation methods were systematically tested. Among them, the calibrated foam material model generally yielded the highest waveform correlation with physical test results, achieving WIFac values typically above 70% across the tested velocities. By contrast, plastic strap fixation and alternative foam models resulted in lower WIFac values, often below 60%. A nonlinear inverse relationship was observed between the tube's Young's modulus and the resulting peak pressure, with 0.001 GPa providing the closest match for the advanced dynamic test. This is physically consistent, as lower stiffness allows for greater deformation and a more gradual pressure increase. Sensitivity analysis was performed by introducing small perturbations in initial velocity and impactor position to evaluate the model's robustness. Results showed that the waveform structure remained stable under moderate variations, supporting the model's reliability within expected test tolerances. Therefore, the calibrated foam model is recommended as the reference configuration for simulation-based evaluations of AHLS pressure tube systems.

To explore the model's applicability in more complex scenarios, additional simulations were conducted using the PDI-2 full-leg impactor. These simulations exhibited increased signal deviations, indicating that further refinement is necessary for integration into biomechanical assemblies. Future work should focus on experimental validation of material parameters and extension to full-vehicle implementations.

Keywords: : FE, FEM, Pressure tube, AHLS, WIFac, PDI-2.

Preface

This thesis project is the base for a Master's degree in Mobility Engineering at Chalmers University of Technology. The work has been carried out at Volvo Cars Safety Centre in Torslanda, Gothenburg, Sweden during the spring of 2025.

Acknowledgements

I would like to express my sincere appreciation to all those who supported us throughout my Master's thesis and my studies at Chalmers University of Technology.

I would firstly like to express my deepest appreciation to Volvo Cars and my supervisor **NILS OLOFSSON** for selecting me for this incredible thesis project. His continuous support, thoughtful guidance, and valuable insights have been vital throughout the entire journey, and this work would not have been possible without his dedication and encouragement.

I would also like to sincerely thank **JOHAN IRAEUS** for serving as my examiner and for making this thesis possible through the foundational work that preceded it. His support and involvement have been greatly appreciated throughout the course of the project.

My heartfelt thanks go to **LUIS VELAZQUEZ** and the entire **VRU Team** for the warm welcome and their extensive assistance during my work. In particular, I am thankful to **DANIEL AZIMIFAR**, **VIKTOR KERIC**, and **PABLO MIRA** for their valuable feedback and expertise in ANSA. I am also grateful to **LAMYAE EL BARAKA** for her support related to CAE modeling.

Finally, I wish to thank my thesis partner **MIA IVKOVIĆ** in Linköping University for her dedication and collaboration throughout the project. It has been a truly rewarding and educational journey working together.

Hanying Zeng, Gothenburg, June 2025

List of Acronyms

Below is the list of acronyms that have been used throughout this thesis listed in alphabetical order:

AHLS	Active Hood Lift System
CAE	Computer Aided Engineering
CFC	Channel Frequency Class
Euro NCAP	European New Car Assessment Programme
FE	Finite Element
FEM	Finite Element Method
HIC	Head Injury Criterion
ISO	International Organization for Standardization
NCAP	New Car Assessment Programme
NHTSA	National Highway Traffic Safety Administration
PDI-2	Pedestrian Detection Impactor 2
WHO	World Health Organization
WIFac	Waveform Integrated Factor

Contents

List of Figures

List of Tables

1
Introduction

According to the World Health Organization (WHO), there were 1.19 million road traffic accidents with fatalities in 2021[1]. Over the last decade, road traffic deaths increased by about 1.9% across 34 high-income and middle-income countries monitored by the International Road Traffic and Accident Database (IRTAD)[2]. Of the 1.19 million road traffic fatalities reported annually, more than 50% are among vulnerable road users such as pedestrians, cyclists, and motorcyclists[1]. Pedestrian deaths accounted for 18.4% of all traffic fatalities in 2023 in EU[5]. Head injuries are the most common severe injury for pedestrians which causes 70 percent of the fatalities because the brain is sensitive to trauma, and that even a slight impact on the head can lead to serious injuries. Safe vehicles play a critical role in averting crashes and reducing the likelihood of serious injury[1]. There has been an increase in awareness of pedestrian safety systems in vehicles to reduce pedestrian injuries, especially the head injuries, to prevent the serious consequences of traffic accidents[6].

The advanced vehicle safety system named Active Hood Lift System (AHLS), is one of the devices developed to reduce pedestrian deaths and injuries caused by pedestrian traffic accidents[6][3].The system protects pedestrians from colliding with hard structures such as the engine by raising the hood and increasing the hood's available deformation space.[6]. When a car collides with a pedestrian, the AHLS is triggered within milliseconds based on the signal from the bumper's membrane sensor. In some cases, depends on the collision speed and severity, the pedestrian impact energy can be partially absorbed by the bending deformation of the hood structure before the pedestrian contacts harder underlying components such as the engine. In this system, the piston functions as a retractable hinge pin or a telescoping rod which, when moved by the pyrotechnic actuator, unlocks or pushes the hood mechanism to allow rapid lifting. Pyrotechnic actuator is activated by the sensor signal when the leg collides with the bumper, and the piston is deployed upwards by an explosion. All the elements that constitute the actuating system are rotated to transmit the actuator force in order to lift the vehicle's hood. The pressure tube sensor from Bosch, which includes a flexible silicone rubber tube, is designed to detect collisions with pedestrians. The active engine hood system in the vehicle is able to trigger protective mechanisms within 10-15 msec of the impact of a pedestrian[3].

Crash safety is one of the key considerations in vehicle structure design and is commonly evaluated using Computer Aided Engineering (CAE) tools. Finite Element Analysis (FEA) has been the trend in virtual crash design over the last decade. The predictive capabilities of FEA allow engineers to fully understand a crash event in a virtual environment, thus limiting the number of physical tests that need to be

executed and thus saving costs. The explicit finite element program LS-DYNA is widely recognized for crashworthiness analysis, which is used by manufacturers to simulate crash tests[8].
While CAE simulations is a very CAE simulations are a useful tool for engineers to assist in developing cars and ensuring capabilities in crash scenarios. However, achieving trustworthy results and reliable correlations with physical tests is challenging. This thesis will more deeply study the pressure tube system in both a virtual environment and physical tests using a method with fewer parts than a full car test.

1.1 Aim

The aim of this thesis project is to evaluate the performance of a pressure tube sensor system using Finite Element (FE) simulation and to assess how well the simulation results correlate with physical impact tests, as well as to identify the factors influencing this correlation. To achieve this aim, the following questions were investigated:

1. What factors influence the current FE model's correlation with the tests?
2. How well do the signal outputs from simulated FE-model compare to physical dynamic tests?
3. How well do the results from the simulated PDI-2 impact test correlate with those from the physical test conducted on a real vehicle?

1.2 Limitations

For simulations, car parts like the bumper fasica or bumper beam will not be remodeled, since they already exist. Striking points for the PDI-2 impactor will be limited to the vehicle centre line. There is a limitation for the computation of the pressure as evaluation, since it considers a 1D approximation.

Additionally, the parameter study focuses only on selected material properties of the pressure tube (e.g., Young's modulus) and the contact interaction between the bumper beam and the foam layer. Other physical factors such as temperature effects, detailed impact location variation, and fluid–structure interaction within the tube are beyond the scope of this work.

2
Background

This chapter begins with an overview of finite element modelling. Following this, this chapter will introduce the crash test, frontal crash detection and the active hood lift system(AHLS) for protecting the pedestrian from frontal crash detection. The pressure tube system, which is used to trigger the AHLS, is then described in details. The chapter will also cover one type legform impactor used to simulate pedestrian collisions in both physical and virtual environments.

2.1 Finite Element Method

The finite element method (FEM) is a numerical analysis technique used to obtain approximate solutions to a wide variety of engineering problems. The core concept of FEM lies in the analytical modelling or approximating the solution domain by subdividing it into a collection of finite elements [16].

Different solvers are required depending on the type of problem. Common solvers include implicit and explicit solvers. For crash simulations involving large deformations, explicit solvers are preferred. LS-DYNA, as one of the most widely used crash simulation software, employs explicit time integration to solve the dynamic equilibrium equations at each time step. Owing to the small time increments, it does not require iterative solutions of material and contact nonlinearities within each step, unlike implicit solvers. Therefore, this thesis employs it as the solver.

For preprocessing and postprocessing, ANSA [18] and META [19] were respectively used. ANSA, as the preprocessing software, handles tasks such as geometric import and cleanup, automatic mesh generation, material assignment, and model assembly. META, as the postprocessing software, supports storing simulation results in chart and report formats for effective interpretation. META also supports the creation of animations, allowing visualization of results in a 3D environment.

2.1.1 Young's Modulus

Young's modulus, also known as elastic modulus, describes the elastic properties of solids subjected to tension or compression in only one direction. It is used to quantify a material's resistance to elastic deformation and defines the linear relationship between stress and strain:

$$E = \frac{\sigma}{\varepsilon} \tag{2.1}$$

where:

- E = Young's Modulus
- σ = Tensile Stress
- ε = Tensile Strain

For a given stress input, a higher modulus indicates less deformation.

In physical crash test, the air inside the tube will be compressed when the impactor strikes the bumper with a pressure tube embedded in, causing the pressure change. The pressure signal will be detected by sensors at both ends of the tube and used to trigger the active lift hood safety systems to protect pedestrians.

Young's modulus is expected to influence the mechanical response of the pressure tube. Niu et al. [21] demonstrated that increasing the modulus led to lower computed strain values in the simulation. By changing the stresses and strains, the pressure response can be different. The results suggest that Young's modulus plays a crucial role in the simulation.

According to material property data provided by AZoM, the Young's modulus of silicone rubber typically ranges from 0.001 to 0.05 GPa [20].Therefore, this study selected multiple representative values within this range for finite element simulation to analyze the influence of Young's modulus on pressure response during impact. By comparing and analysing these effects, this study aims to identify a reasonable Young's modulus that not only ensures mechanical realism in the simulation response but also enables the pressure signal output to closely match the physical test results, thereby improving the predictive capability of the FE model.

2.2 Crash Tests

Vehicle crash tests are critical evaluations of a vehicle's collision safety performance. These tests are conducted in a controlled environment under controlled collision conditions and specific load conditions to assess the vehicle's safety performance during a collision. Accelerometers are utilized to collect data during the collision. Furthermore, sensors are installed on human-shaped test dummies, otherwise known as crash test dummies.These dummies are utilized to guarantee the repeatability and reproducibility of tests, as well as to simulate the kinematic responses of humans during car crash.

Currently, a variety of new car assessment programs (NCAP) are operational in Europe, Japan, the United States, and other countries. This thesis focuses on the European New Car Assessment Program (Euro NCAP).In comparison with collision tests conducted for vehicle legal certification design, NCAP employs more stringent collision tests to evaluate vehicles. The Euro NCAP utilizes a 1-to-5-star rating system, with 5 stars indicating the highest level of safety. Vehicles that merely meet legal certification standards typically do not receive any stars in Euro NCAP tests.However, achieving a 5-star rating from Euro NCAP signifies that the vehicle manufacturer has considered the safety of pedestrians and occupants. Consequently, vehicles that have received a 5-star rating are more likely to appeal to consumers who

prioritize safety. This is one of the rationales why manufacturers execute simulated collision tests during the preliminary design phase to substantiate or discard design concepts based on the outcomes of these tests[25].

These tests are designed to evaluate vehicle performance under standardized impact conditions that approximate common crash configurations, such as full-scale collisions with fixed barriers. Additionally, subsystem tests, including pedestrian impact scenarios, are conducted to assess the safety performance of the vehicle's front-end structure. The assessment of collision risks involves the calculation of injury risks using acceleration, force, displacement, and other data collected by sensors during the collision. This facilitates the assessment of potential injuries to human occupants in such a scenario. It is essential to ensure that the risk of injury remains below a certain threshold to ensure successful completion of the certification process. The injury criteria used to calculate injury risks are derived from tests on cadaver specimens and real collision reconstructions[26]. Although crash test dummies are continuously being improved to achieve higher levels of biometric fidelity and realism, this progress also introduces greater complexity.

2.3 Frontal Crash Detection

Traffic accidents remain the leading cause of death and injury. Research indicates that during pedestrian collisions, the head and lower limbs are the most commonly injured areas[22], with the front of the car being the first point of contact.

Automotive manufacturers have developed a range of pedestrian protection systems to reduce the injury risk. These systems can be categorized into active safety systems and passive safety systems. According to the Haddon Matrix, active safety systems operate during the pre-collision phase, aiming to prevent collisions from occurring, while passive safety systems activate during or immediately after a collision, aiming to reduce the severity of injuries when a collision is unavoidable[27].

Research indicates that driver error accounts for over 90% of collision accidents[28]. Many active safety systems can issue warnings 1–2 seconds or even earlier before a potential collision occurs, assisting drivers in taking timely corrective actions such as braking, decelerating, or steering maneuvers. Furthermore, if the driver does not respond in time, some systems can automatically apply braking to mitigate or avoid a collision.

Although active detection systems have significant preventive effects, collisions may be unavoidable under certain conditions, such as low visibility, complex urban environments, sensor obstruction, or insufficient reaction time. This emphasizes the necessity of passive safety measures specifically designed to mitigate injuries in unavoidable collisions.

2.4 Active Hood System

AHLS works by triggering pyrotechnics or spring-loaded actuators and raise the rear end of the bonnet by approximately 70 to 110 millimetres. It prevents the pedestrian's head from direct impact with engine block or windscreen base. Research indicates that during headform impact tests, the application of AHLS can significantly reduce the Head Injury Criterion (HIC). When deployed at 40 km/h during a collision, AHLS can reduce HIC values by up to 90% and may reduce fatal head injuries in up to 80% of applicable cases[3]. In addition, a comprehensive analysis of Euro NCAP pedestrian protection test results found that vehicles equipped with pop-up hoods achieved an average headform score of 17.2 out of 24, compared to 13.8 for vehicles without this feature, demonstrating a clear improvement in head protection performance under standardized conditions[4]. While the real-world impact still requires further study, these experimental and statistical results together support the benefit of AHLS in mitigating severe head injuries in unavoidable pedestrian collisions.

The most critical factor for AHLS effectiveness is the response time during the initial collision phase. If the system deploys too slowly, there may be insufficient time to lift the bonnet fully before the pedestrian's head impacts the vehicle, limiting the available deformation space to absorb kinetic energy. As a result, the protective effect is reduced because the head impact energy cannot be adequately dissipated.

Various sensors (such as accelerometers, contact switches, or radar-based systems) have been used to detect pedestrian collisions. Modern vehicles are increasingly adopting pressure-based detection systems. The pressure tube sensor from Bosch used in this thesis can trigger AHLS or similar protective functions within a 10–15 millisecond window, offers. The technical structure, operating principle will be detailed in 2.5.

2.5 Pressure Tube System

To ensure that the Active Hood Lift System (AHLS) activates promptly, the vehicle must reliably detect a pedestrian collision within milliseconds of the impact. The pressure tube sensor system is a cost-effective and reliable solution.

A widely used implementation of this principle is Bosch's pressure tube sensor system, which is described in detail below and serves as the basis for the simulation in this study. It consists of an elastic silicone tube filled with air, which is integrated into the vehicle's front spoiler. At each end of the tube, two pressure sensors are mounted to monitor the pressure inside the tube. When frontal crash happens, the tube compresses at the point of impact, generating a pressure wave that propagates through the air inside the tube. The pressure changes at both ends of the pressure tube are interpreted by the control unit via the PSI5 interface, which handles data transmission and power supply. The control unit analyzes the pressure signal curve to confirm a valid collision. After verification, it triggers protective mechanisms, such as an active hood lift system within 10 to 15 milliseconds of initial contact.[6]

In this thesis, the sensor's behavior is modeled using LS-DYNA's keyword *DEFINE_PRESSURE_TUBE which simulates an air-filled pressure tube based on a one-dimensional acoustic wave propagation model derived from the compressible Euler equations[26]. The shell-based modeling method is used in this thesis, internal pressure is calculated based on the cross-sectional area that changes over time and space, which in turn is derived from the node displacement of the shell elements. The propagation of pressure waves is described by a one-dimensional acoustic approximation equation of the compressible Euler equations.

$$(Ap)_t + p_0(Au)_x = 0 \tag{2.2}$$

$$(Au)_t + \frac{Ac^2 p_x}{p_0} = 0 \tag{2.3}$$

$$c = \sqrt{\frac{p}{\rho}} \tag{2.4}$$

$$p_{tt} = c^2 p_{xx} \tag{2.5}$$

Here, A is the tube cross-sectional area, p is the local gas pressure, u is the gas velocity along the tube axis (x-direction), p_0 is the steady-state reference pressure, c is the speed of sound in the tube gas (typically air), and ρ is the gas density. The subscripts t and x denote partial derivatives with respect to time and the tube's axial coordinate, respectively. For example, $p_t = \partial p/\partial t$ and $p_{xx} = \partial^2 p/\partial x^2$.

By reproducing the physical response of sensors in a virtual environment, this simulation framework can analyze the generation and propagation of pressure waves inside pipes during frontal crashes.

2.6 Impactors

When frontal crash happened with pedestrians, legs typically make initial contact with the front bumper, which directly affects the triggering mechanism of detection systems.

Legform impactors are therefore widely used. They are intended to replicate the kinematic and biomechanical responses during impact and recreating the process in physical tests. In this thesis, for FE simulation, legform impactors are used to assess whether the advanced FE model can better replicated the physical scene. The primary focus of this thesis is not on developing the legform impactor setup itself, but on using its simulation-to-test correlation as a benchmark reference to evaluate the accuracy and consistency of the advanced FE model developed in this study. This approach enables the evaluation of the extent to which advanced FE models are capable of reproducing physical test conditions. This comparison is used to determine the necessity of further validation of the models and get a better understanding on which factor are most critical to optimize in order to achieve better alignment between virtual simulations and real crash scenarios.

2.7 PDI-2

The Pedestrian Detection Impactor 2 (PDI-2) is developed to evaluate contact sensor systems in equipped with deployable pedestrian protection systems, such as Active Hood Lift Systems (AHLS). Specifically it is designed to represent "hardest-to-detect" scenarios for sensor triggering across various vehicle types, including SUVs.

The PDI2 impactor is designed to replicate what is referred to as the Hardest to Detect Pedestrian in EuroNCAP testing scenarios for test a car's ability to detect pedestrians. The leg form merely serves as an impactor object and does not record any injury criteria, as it sole purpose is to serve as an impactor for detection capabilities of a car. The relative impact speed range for vehicle front-end structures tested with PDI-2 is 20 km/h to 40 km/h. It features a carbon fiber tube core, with a steel core and lead core wrapped inside, and a highly durable foam outer shell. The PDI-2 features a lightweight construction and operates reliably within a temperature range of –30°C to +70°C. It is capable of withstanding repeated tests at speeds of up to 55 km/h. PDI-2 is suitable for both full-scale crash testing and propulsion-based setups. In FE simulations, PDI-2 models are available in widely used software such as LS-DYNA, Abaqus, and Radioss[29].

Standardized PDI-2 FE models have been widely applied in crash simulations and are primarily validated at the component and sub-system levels under controlled conditions, including impactor mass, stiffness, and force–time characteristics for typical front-end structures (sports cars, sedans, SUVs) [30]. Pal et al. further performed full-vehicle tests and found good correlation with simulations during the loading phase, with minor deviations in rebound [31]. Overall, the PDI-2's full-vehicle validation remains limited and depends on specific front-end designs; discrepancies can result from the impactor's simplified geometry and from structural modeling uncertainties [30, 31].

In this study, the PDI-2 is used as a practical reference to assess whether the advanced FE model captures the key trends in sensor signals observed in physical tests. Considering its validation status, this serves as an indicative check rather than an absolute benchmark, guiding potential areas for further improvement in the simulation framework.

3
Methods

In this chapter, methods related to simulation and verification are described to achieve the research objectives. In order to evaluate the FE pressure tube model, two simulation settings were employed. The first setup is a highly simplified model, which is built and tested as the foundational starting point. The second setup is more complex and closer to the real structure of a vehicle compared to the simplified one. The relatively complex model has never been previously tested, therefore, a similar setup was built in physical tests to obtain comparable data.

Two simulation model's construction and configuration have been informed by prior tests conducted by Dynamore and Volvo Cars.

3.1 Building the simplified FE model

The first phase focused on developing a simplified simulation model to become familiar with the tools ANSA and META. This model was designed to evaluate the behavior of a basic pressure tube under compression. It consists of a ground(1), a cylinder-shaped impactor(2), a foam block(3), a pressure tube(4), and two sensor placeholders(5). The layout of the simulation model is shown in Figure 3.1.

To replicate realistic conditions, specific boundary conditions were applied in simplified test model. The ground and sensors were fully constrained in all directions, the impactor was constrained in X-Y direction and allowed to move only in the Z-direction. The foam block was free in all directions. The ends of the pressure tube were connected to the sensors through nodes, thereby ensuring their fixed position.

Component contact were modeled using the `*CONTACT_AUTOMATIC_SINGLE_SURFACE` keyword, allowing contact between all parts. A gravitational load of 9.81 m/s^2 was applied to every component. The mesh used quadratic elements with size of 3.4 mm. The mesh size in the simplified model was selected based on the balance between computational cost and solution accuracy.

It is important to note that the modeling of the pressure tube itself was not developed from scratch in this thesis. For the purpose of this thesis, the pressure tube FE model was refined by extending the geometry and by tuning parameters such as the silicone tube's Young's modulus, the foam's material card and the contact between foam and bumper. In this simplified setup, the sensors operated as fixed geometrical constraints, with no contribution to pressure calculation.

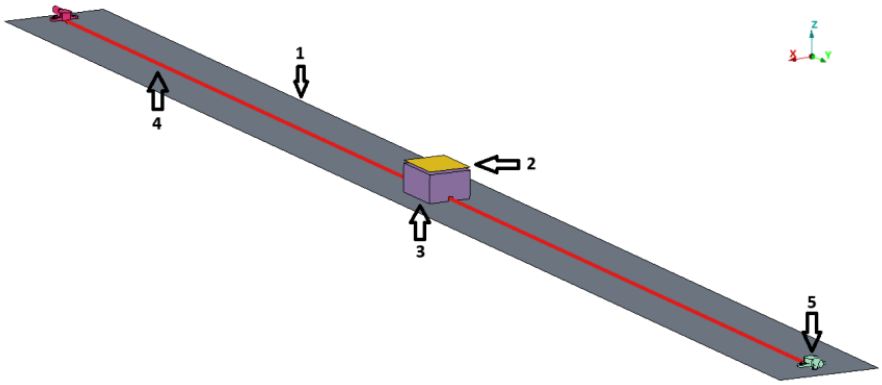

Figure 3.1: Simplified test setup used in the simulation.

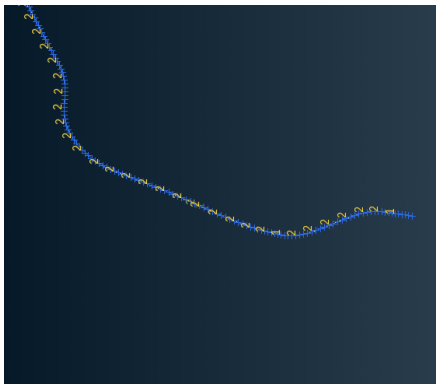

(a) Beam elements

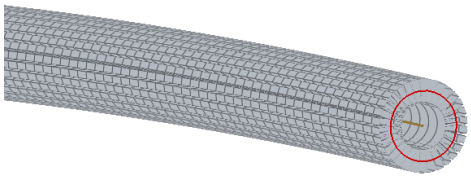

(b) Surrounding shell elements

Figure 3.2: Beam and shell elements used in the pressure tube model.

The pressure tube has a total length of 2570 mm. It was initially modeled using beam elements, and shell elements were added to represent its outer geometry. The material is silicone rubber. The foam component, identified as ARPRO (expanded polypropylene), is commonly used in automotive applications to hold the tube in position. The foam was modeled using solid elements. Other components used shell elements. Table 3.1 lists the material properties used in the simulation.

Table 3.1: Material properties for components in the simplified test setup.

Component	E [GPa]	ν	ρ [kg/mm^3]	c [mm/ms]	p_0 [GPa]
Ground	210	0.30	7.85×10^{-6}	–	–
Impactor	210	0.30	1.736×10^{-4}	–	–
Foam	0.0106	–	3.04×10^{-8}	–	–
Pressure Tube	0.00223	0.49	2.30×10^{-6}	340	0.0001
Sensors	210	0.30	7.85×10^{-6}	–	–

This simulation model is based on a simplified physical test that Volvo Cars performed in collaboration with DYNAmore in 2018. The original test was used as a

reference to correlate the simulation's behavior under controlled conditions. The setup of the physical test is shown in Figure 3.3.

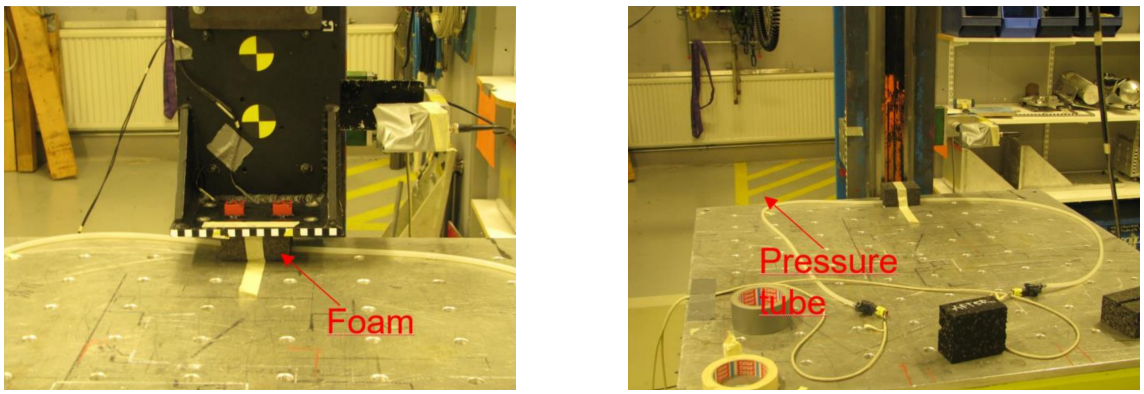

(a) Foam compression **(b)** Complete test setup

Figure 3.3: Physical testing performed by Volvo Cars in 2018.

3.2 Building the advanced FE model

The simplified model is an effective starting point, however it lacks several key structural features found in actual vehicle configurations. To achieve a higher level of fidelity and more realistic pressure signal behavior, an advanced finite element model was developed.

The advanced setup includes key front-end structural components of vehicles, such as the bumper beam, foam, pressure tubes, sensors, and impactors, shown in Figure 3.4. Note that only the listed structural components were modeled; the fascia and other exterior surfaces were excluded in this study. The objective is to more accurately reproduce the mechanical interactions and constraints that influence pressure propagation during the impact process.

The boundary conditions and contact definitions for the advanced model were defined using knowledge gained from the simplified test model. Similar to the simplified setup, sensors at both ends of the tube were incorporated to ensure geometric fidelity. The two sensors constrain the tube ends, but do not actively compute pressure.

As shown in Figure 3.4, two sensors are fixed in place, the impact body is free to move only in the Z direction, while the bumper beam is fixed only at the bottom. The foam and the rest of the bumper are free in all directions. All components are pre-existing models that have already been created. except for the impactor.

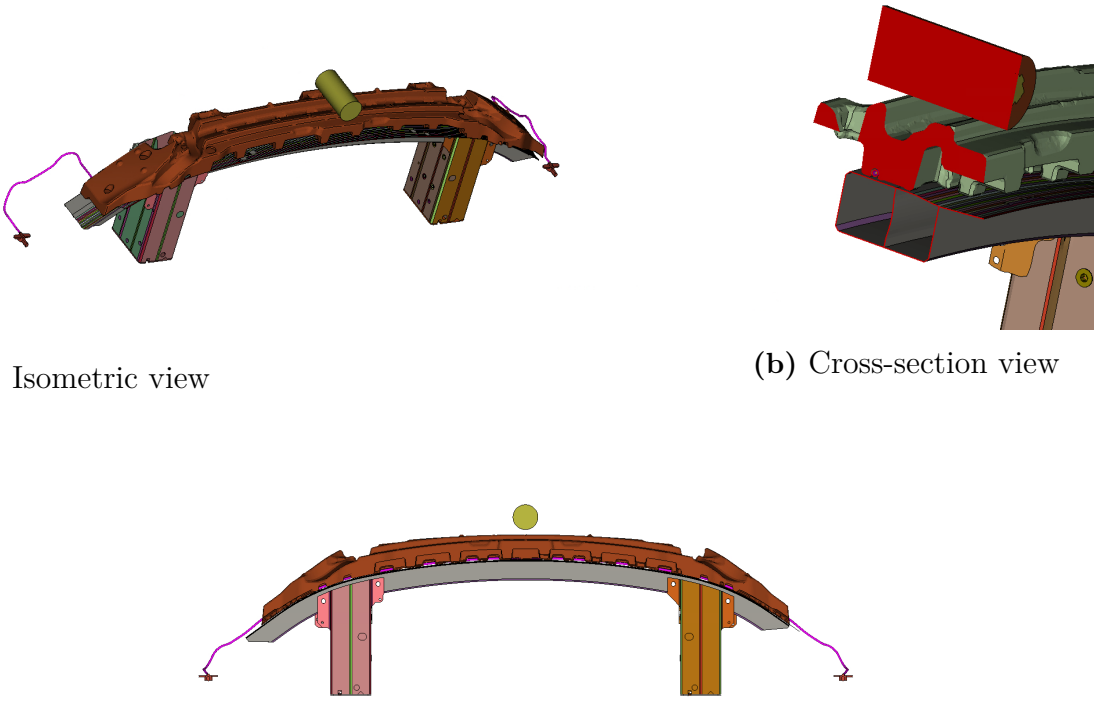

(a) Isometric view

(b) Cross-section view

(c) Front view of the sensor setup

Figure 3.4: Different views of the advanced setup

Two contacts were defined to ensure the foam stays in place, while in the physical test the foam was fixed with tape or stripes. In the FE model, this attachment was simplified by contacts only, without explicitly modeling the tape or stripes.

- `*CONTACT_AUTOMATIC_SINGLE_SURFACE`: This contact is analogous to the one employed in the simplified model, ensuring that all components are in contact and exert influence on one another.
- `*TIED_NODES_TO_SURFACE_CONSTRAINED_OFFSET`: This contact was utilized to model the interaction between the foam and the bumper beam.

Before the contact was defined, the foam was inspected to identify the areas where it makes contact with the bumper beam. As shown in Figure 3.5, these contact regions were marked and converted into a set of nodes for contact definition. The red areas in the figure represent the identified foam regions that are in contact with the upper surface of the bumper, which is shown in blue. These nodes were then tied to the beam using contact constraints, allowing them to behave in the same way as the bumper surface. This ensures that the foam stays in place during impact while still allowing for realistic deformation and vibration as would be expected in real-world conditions.

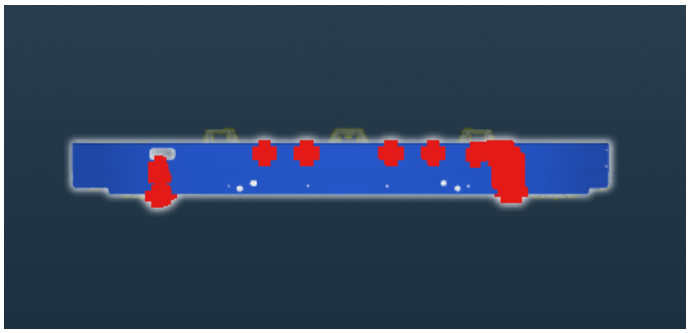

Figure 3.5: Identified contact points between foam and bumper beam

The impact velocities used in the simulation were 2.5, 3, and 4 m/s. These values were selected based on information from the sensor manufacturer indicating that the sensor system typically activates at an internal tube pressure of 25 mbar, corresponding to an impact velocity of approximately 25 km/h. Since this value was not verified directly for the specific setup used in this thesis, a range of lower velocities was selected for the simulation to identify the most representative conditions of the sensor triggering threshold. The impactor is made of aluminum with a total mass of 7.95 kg, it has a radius of 70 mm, a length of 148 mm. These values were based on the actual components in physical testing, as described in the following section 3.3.

Two foam material cards were implemented in the simulation.The difference in the two material cards is due to the different testing procedures used by different laboratories. Although the same base material was used for testing, the strain rate ranges were slightly different. The two foams were simulated to determine which could most accurately replicate actual behavior. For simplicity, this thesis refers to the two foams as **Material 1** and **Material 2**.

To correlate how well the materials replicated the real setup, the impactor's velocity, displacement, and acceleration were compared against measured results. Additional material properties used in the simulation are presented in Table 3.2. The mesh for the foam consisted of tetrahedral elements, while a quadratic mesh of 3.4 mm was used for all other components. The foam was modeled using LS-DYNA's *MAT_FU_CHANG_FOAM (MAT83), which describes the nonlinear compressive behavior of closed-cell foams.

To identify the parameters most influencing the pressure behavior inside the tube, a variation study was conducted by adjusting certain material parameters. Although the pressure tube material is known to be silicone rubber, the material properties such as Young's modulus were not officially provided. Although silicone rubber exhibits nonlinear, hyperelastic behavior and generally undergoes significant deformation to produce a clear pressure transient, some test cases with lower impact severity result in a weaker pressure response and more moderate deformation. In this study, a linear elastic approximation was adopted as a practical simplification due to the lack of reliable hyperelastic data and to maintain numerical stability in these low-pressure cases.

Values for Young's modulus, Poisson's ratio, and density were obtained from literature, manufacturer data, and online engineering forums. Based on these sources, simulations were performed iteratively using different combinations of parameters until a satisfactory match with the expected behavior was achieved, where "satisfactory" means reproducing a similar peak value and overall pressure–time curve shape. Initial simulations used Young's modulus values across the full literature range of 0.001–0.05 GPa to investigate its effect on the pressure response. Based on preliminary results, significant changes in peak pressure were primarily observed when the modulus was below 0.01 GPa. Therefore, the subsequent parameter tuning focused more finely within the 0.001–0.01 GPa interval to better match the physical test data. The final properties selected for the pressure tube are shown in Table 3.1.

Table 3.2: Material properties of simulation components.

Component	E (GPa)	ν	ρ (kg/m^3)	c (mm/ms)	p_0 (GPa)
Bumper	70	0.30	2700	–	–
Foam	0.0106	–	30.4	–	–
Impactor	70	0.30	2700	–	–
Pressure Tube	0.001	0.49	2300	340	0.0001
Sensors	210	0.30	7850	–	–

3.3 Physical test

As the simplified model had previously been tested by Volvo Cars, this test was repeated in this work following the same setup (Figure 3.3) to ensure consistency. Physical tests were also conducted for the advanced model, and the comparison will be discussed in the Result section.

The components used in this advanced model are shown in Figure 3.6. It includes the bumper beam (1), foam (2), pressure tube (3), sensors (4), and impactor (5).

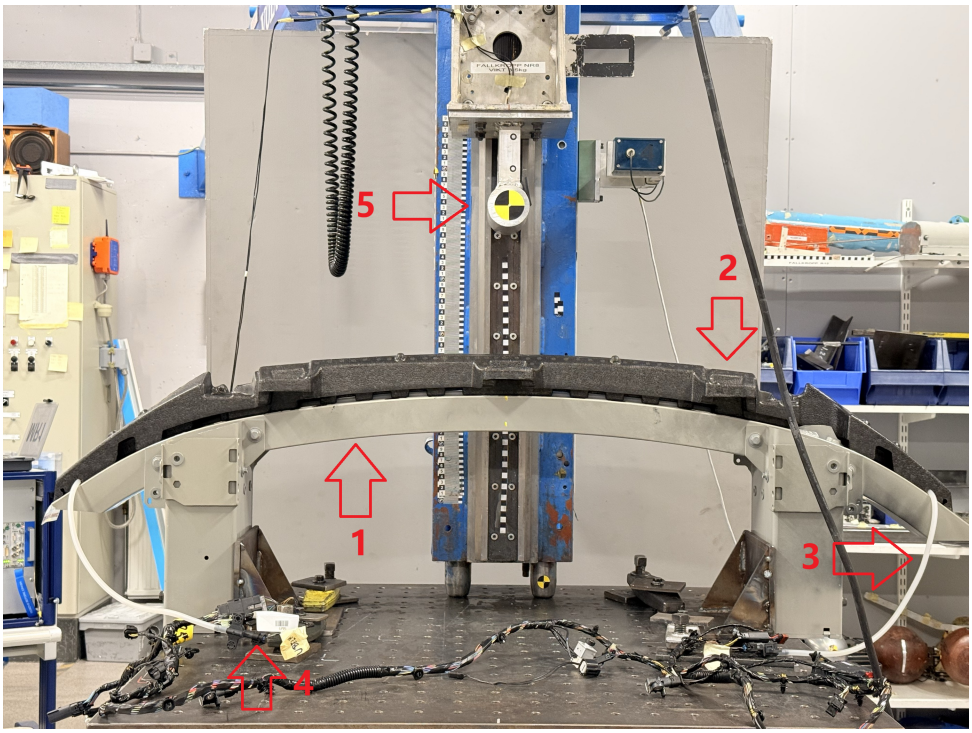

Figure 3.6: Physical testing for the advanced setup.

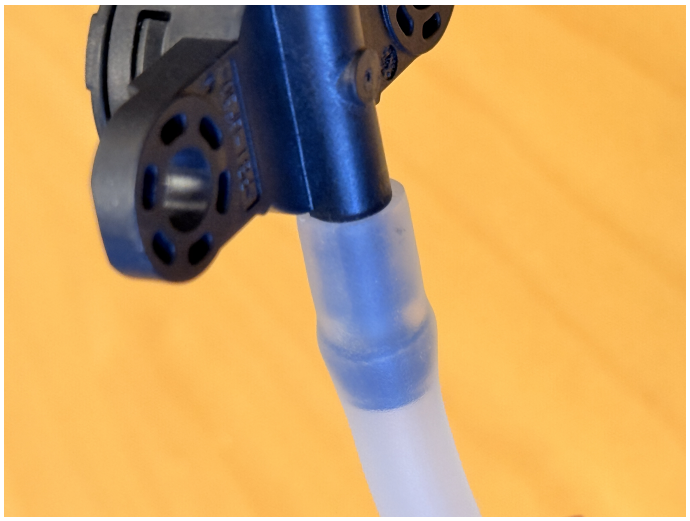

Figure 3.7: Tube–sensor plug connection

To reflect the physical configurations, simulations for both Material 1 and Material 2 included equivalent foam constraint conditions that approximate the effects of the tape and plastic stripes used in the physical tests. The same quantities (2 or 4) and impact velocities (2.5, 3.0, and 4.0 m/s) were considered, as discussed in Section 3.1. The impactor is made of aluminum with a total mass of 7.95 kg, it has a radius of 70 mm, a length of 148 mm. Physical tests were then conducted to correlate the accuracy of these simulations. The simulations aimed to examine whether the internal tube pressure could reach the manufacturer-specified sensor

activation threshold of 25 mbar. Since this threshold is typically associated with higher vehicle impact speeds such as those used in the PDI2 test (approximately 7 m/s), a lower range of impact velocities was chosen here to study the system response under moderate conditions.

Physical tests were first conducted at 3 m/s (10.8 km/h). The results showed that the internal pressure exceeded the expected threshold. Based on these results, the speed was lowered to 2.5 m/s (9 km/h), and the results showed that the pressure approached 25 mbar. Subsequently, the speed was increased to 4 m/s (14.4 km/h) to explore the effects of higher impact energy.

Another key consideration in this physical testing setup was how to attach the foam component to the bumper. In the realistic situation, the foam does not rest directly on the bumper in a vehicle; instead, it is suspended by being hooked onto the front bumper cover at two points, allowing it to hang freely with only slight contact with the bumper.

To simplify the testing procedure while preserving functional realism, the foam was placed directly on top of the bumper. However, leaving the foam entirely free on the surface posed a risk of its sliding during impact, which could lead to inconsistent test results.

To address this, a set of restraining methods was introduced. Masking tape and plastic stripes were applied at points approximating the hooks in the bumper fascia and additionally at the foam edges to prevent excessive bending. This arrangement limited undesired movement while still allowing the foam to deform and rebound locally. The two methods preserved partial freedom of foam's movement while ensuring foam's stability during the impact. The types of restraints and test configurations are summarized in Table 3.3 and illustrated in Figure 3.8.

The tests were completed within three days. Each test was repeated twice, except for the 2.5 m/s impact test (using four strapes), which was performed three additional times. These settings was based on the positive results obtained in the initial test, and the additional tests were conducted to correlate the test results. For all repeated test configurations, the results were averaged to reduce variability. After each test, the test results were sent to Bosch for signal processing. After the original signal data being converted into a readable format, the data was sent back for further analysis. Acceleration, velocity, and displacement of the impactor were also measured during the physical test. For ease of analysis, data from the left and right sensors were processed separately to identify potential side-specific behaviors.

Table 3.3: Foam restraint configurations in physical impact tests.

Test	Strapes	Type	Velocity (m/s)	Description
1	2	Masking tape	2.5	2 tape strapes placed between crashboxes
2	2	Plastic strapes	2.5	2 plastic strapes placed between crashboxes
3	4	Masking tape	2.5	2 tape strapes between crashboxes, 2 outside strapes
4	4	Plastic strapes	2.5	2 plastic strapes between crashboxes, 2 outside strapes
5	2	Masking tape	3.0	2 tape strapes placed between crashboxes
6	2	Plastic strapes	3.0	2 plastic strapes placed between crashboxes
7	4	Masking tape	4.0	2 tape strapes between crashboxes, 2 outside strapes
8	4	Plastic strapes	4.0	2 plastic strapes between crashboxes, 2 outside strapes

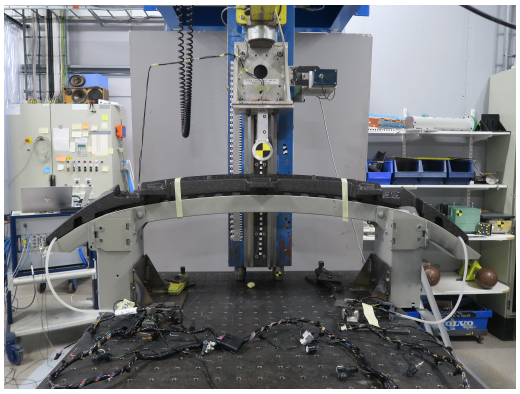

(a) 2 masking tapes

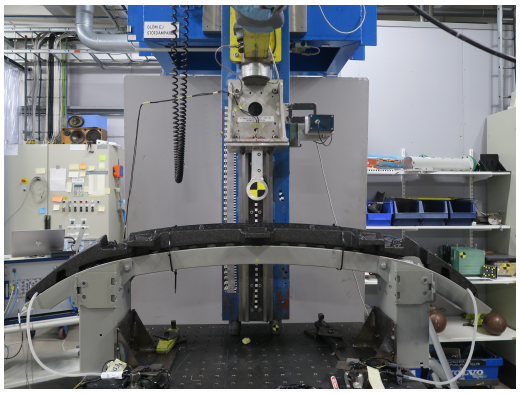

(b) 2 plastic strapes

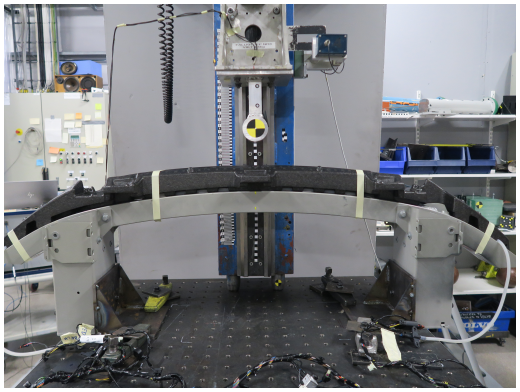

(c) 4 masking tapes

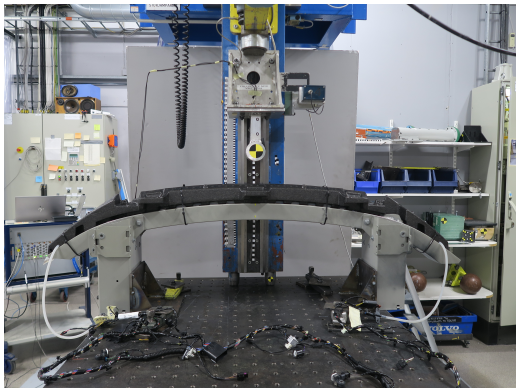

(d) 4 plastic strapes

Figure 3.8: Physical test configurations with different foam restraint methods.

3.3.1 Physical test with PDI-2

A simulated test was conducted using the PDI-2 leg impactor to compare its pressure response with that from pedestrian impact tests. The pressure tube retained the same assumed material properties (Table 3.2) as used in both the simplified and advanced configurations. All components used in the FE simulation were existing models provided by the Volvo Car Corporation. The assembly details of this model in both the FE simulation and the physical test cannot be disclosed.

The physical test setup for this included the front structure of a fully equipped vehicle, with the PDI-2 impactor positioned in front of the vehicle to subsequently collide with it. The comparison results will be presented in Chapter 4.

A reference illustration of this procedure is shown in Figure 3.9 below, based on the Euro NCAP guideline, it does not represent the actual setup used in this thesis. The general principle of the impactor release and free-flight configuration follows the standard methodology.

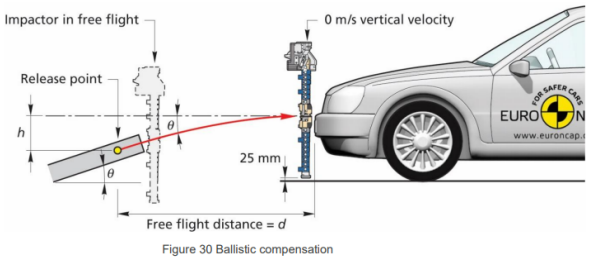

Figure 3.9: Ballistic compensation principle (reference only)

3.4 Sensitivity analysis

A sensitivity analysis was conducted to determine which parameters in the advanced FE model have the greatest impact on simulation results. The objective was to determine whether the results would deviate significantly or remain within acceptable limits under different conditions. Three sensitivity tests were conducted with minor adjustments to parameters such as the impactor's velocity, position, and rotation. In each test, only one parameter's baseline value was altered.

The analysis was performed using the material of foam with the best correlation to physical test results. The primary objective was to assess whether small deviations in input parameters would cause significant changes in simulation outputs. The specific parameter changes used in the sensitivity analysis are summarized in Table 3.4.

Table 3.4: Sensitivity analysis parameters(based on Euro NCAP variation limits)

Description	Variation	Unit
Impactor's velocity	±2	%
Impactor's position	±10	mm
Impactor's angle	±2	Degrees (°)

3.5 Signal processing

This section introduces the signal processing work carried out during the project. After the model was preprocessed in ANSA, the simulation was carried out using LS-DYNA. The results were then post-processed and analyzed in META. The main focus was extracting the required output curves for this thesis and filtering and comparing them using the appropriate analysis tools.

3.5.1 Simulation post-processing

To enable meaningful comparison between simulation results and physical test results, all raw signals were processed to reduce noise while preserving relevant characteristics.

The processed physical test data includes pressure and acceleration signals. The pressure signal was recorded using sensors from Bosch. These sensors have built-in hardware-level filtering functionality, no external post-processing filters were applied to this data, which results in smoother output curves compared to unfiltered simulation curves. The acceleration curve was derived in META by numerically differentiating the velocity signal obtained from the physical test and provided by the lab. All curves were filtered using a channel frequency classification (CFC) filter in accordance with ISO 6487 standards. Acceleration, velocity, and displacement curves were filtered using a CFC 1000 filter. The pressure signal is filtered using a CFC 180 filter to match the effective smoothness of the Bosch sensor output after hardware filtering.

After the simulation is complete, the acceleration, velocity, and displacement curves can be obtained directly in META. In our simulation, the acceleration data obtained directly from LS-DYNA exhibited numerical noise. Therefore, the acceleration curve was recalculated by performing numerical differentiation on the velocity output, which is consistent with the method used to process physical test data.

To ensure time alignment, the simulation curves are trimmed and shifted so that the time origin coincides with the point where the pressure signal shows a clear increase above approximately 2–3 mbar, matching the physical test signal. All processed signals are normalized to start at zero for visual comparison and curve overlay.
For each test configuration, the simulation results were plotted alongside the corresponding averaged physical measurements to enable visual comparison. Simulation pressure signals were compared with actual sensor signals to assess model fidelity under varying restraint types, impact speeds, and foam materials cards.

3.5.2 Curve comparison using WIFac

The Weighted Integrated Factor (WIFac) was employed to evaluate the similarity between the simulated data and physical test data in this thesis. This approach complemented the visual comparisons by providing a numerical metric of agreement. This method was selected due to its availability as a built-in comparison tool in META, as well as its ease of implementation in Python, which allowed for automation of the comparison workflow. It provides a simple and consistent numerical metric for assessing overall curve similarity, which is useful for evaluating pressure response trends. WIFac quantifies the overall similarity in curve shape between two time-dependent signals, returning a score between 0 and 1, where 1 represents a perfect match. It was applied independently to each test configuration to assess waveform similarity in pressure signals.

Unlike simple peak or time comparisons, WIFac integrates shape similarity across the entire time domain. The mathematical expression of WIFac is shown in Equation 3.1.

$$\text{crit} = 1 - \frac{\sqrt{\int_t \max\left(|f(t)|, |g(t)|\right) \cdot \left(1 - \frac{\max(0, f(t) \cdot g(t))}{\max(f(t)^2, g(t)^2)}\right)^2 \, dt}}{\int_t \max\left(|f(t)|, |g(t)|\right) \, dt} \tag{3.1}$$

WIFac values range from 0 to 1, this report presents them as percentages for improved readability. It is important to note that for this particular application, there is no clearly established threshold for what constitutes a “good” WIFac score. However, based on general guidelines and experience, values around 0.6 can be acceptable for exploratory simulations, while more rigorous applications may require scores above 0.8.[32].

4

Results

This chapter presents the results of the physical tests and their comparison with FE simulations. First, the overall kinematic responses of the impactor—including acceleration, velocity, and displacement—are analyzed to verify the consistency of the global motion. Next, the local pressure signals at three different impact velocities are compared, and the similarity between the simulated and measured results is quantified using WIFac values. Based on these results, a sensitivity analysis is conducted to evaluate the model's response to variations in initial conditions. Furthermore, the correlation between the simulated PDI-2 responses and the physical vehicle front-end tests is discussed. Finally, the influence of different Young's modulus settings for the pressure tube on the simulation results is analyzed.

4.1 Impactor kinematic response

This section begins by evaluating whether the material models and boundary conditions can reproduce the overall kinematic behavior of the system, which provides the physical basis for interpreting the local pressure signals discussed later. To this end, acceleration, velocity, and displacement data are extracted from a node at the top of the aluminium impactor, corresponding to the sensor location used in the physical test, and are compared across different impact velocities.

This section is to comparing simulated and physical test curves at three different impact velocity in order to correlate the consistency of each material model with the actual dynamics. WIFac correlation analyses were also conducted for each parameter.

4.1.1 Acceleration

Figure 4.1 presents the acceleration curves at three impact speeds. While both materials underestimate the peak values and reach them earlier than the physical test, Material 2 demonstrates a visibly better match in curve shape and timing. Material 1 shows a steeper initial drop and faster unloading across all speeds.

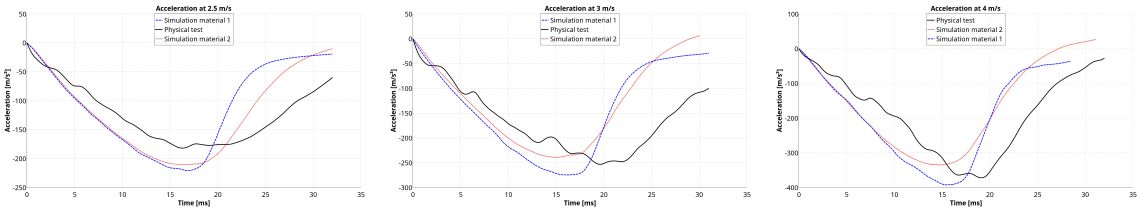

(a) Acceleration curves at 2.5 m/s

(b) Acceleration curves at 3 m/s

(c) Acceleration curves at 4 m/s

Figure 4.1: Acceleration responses at different impact speeds

Table 4.1 presents the WIFac values across different velocities. Material 2 shows increasing WIFac values as the impact velocity increases, reaching its highest value at 4 m/s. In contrast, Material 1 remains below 63% across all tested speeds. The difference in WIFac values between the two materials becomes more pronounced at higher velocities.

Table 4.1: Correlation analysis of acceleration

Material	Speed (m/s)	WIFac (%)
1	2.5	62.0
1	3.0	58.9
1	4.0	58.8
2	2.5	72.8
2	3.0	68.9
2	4.0	73.3

4.1.2 Velocity

Figure 4.2 presents the velocity curves at three impact speeds. It can be noticed that both simulation materials replicate the general deceleration trend observed in the physical tests. The velocity begins at the intended initial impact speed and gradually decreases to negative values, reflecting the rebound phase.

Both materials demonstrate a strong correlation with the physical test curve at 2.5 m/s and 3.0 m/s within 15 ms. After 15ms, Material 1 tends to unload faster, while Material 2 maintains a more gradual slope, following the physical deceleration more closely. At 4.0 m/s, this divergence becomes more apparent: both materials predict a faster drop in velocity, but Material 2 again shows a closer alignment over a longer time period.

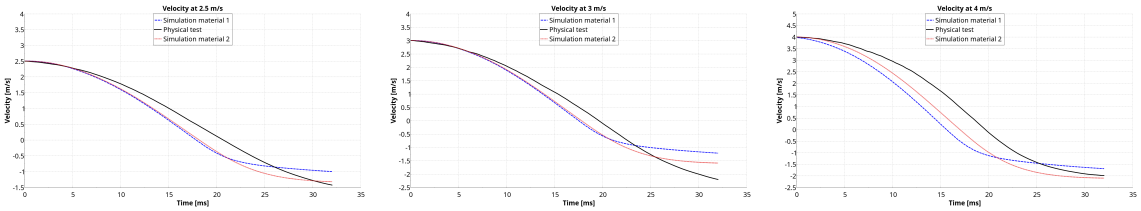

(a) Velocity curves at 2.5 m/s **(b)** Velocity curves at 3 m/s **(c)** Velocity curves at 4 m/s

Figure 4.2: Velocity responses at different impact speeds

As shown in Table 4.2, observations above are confirmed. The WIFac correlation values in Material 2 achieve a higher correlation at all speeds, with the strongest match occurring at 3.0 m/s (85.5%). Material 1 performs worse than Material 2, and its accuracy declines at higher speeds.

Overall, the velocity response results show that Material 2 provides more consistent and reliable agreement across the full range of impact conditions.

Table 4.2: Correlation analysis of velocity

Material	Speed (m/s)	WIFac (%)
1	2.5	81.8
1	3.0	78.5
1	4.0	70.8
2	2.5	82.9
2	3.0	85.5
2	4.0	78.6

4.1.3 Displacement

As shown in Figure 4.3, the displacement curve of the impactor reveals consistent trends across all impact speeds. In every case, the physical test curve shows slightly higher peak displacement than the simulation materials. This suggests that materials 1 and 2 tend to underpredict the system's deformation slightly.

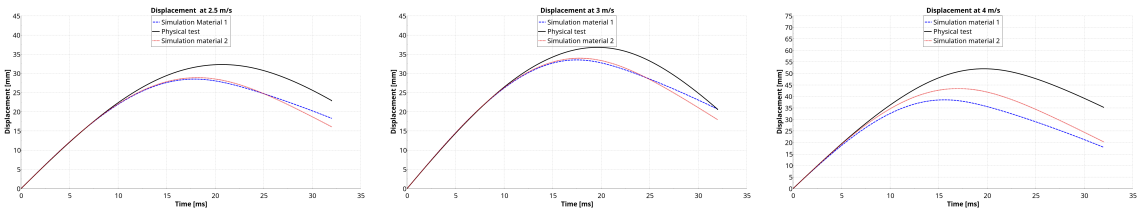

(a) Displacement curves at 2.5 m/s **(b)** Displacement curves at 3 m/s **(c)** Displacement curves at 4 m/s

Figure 4.3: Displacement responses at different impact speeds

We can notice that both materials provide similar curve shapes at 2.5 m/s and 3 m/s. Both of them achieve high WIFac scores above 84%, as seen in Table 4.3.

At 4 m/s, Material 2 remains closer in shape and timing, leading to a significantly higher WIFac value of 77.9%, compared to 68.7% for Material 1. Material 1 shows a notably lower displacement peak and a steeper unloading slope compared to the physical test.

Table 4.3: Correlation analysis of displacement

Material	Speed (m/s)	WIFac (%)
1	2.5	85.7
1	3.0	90.7
1	4.0	68.7
2	2.5	84.7
2	3.0	90.1
2	4.0	77.9

4.2 Pressure comparison

This section aims to evaluate the ability of the simulation to accurately capture key stress characteristics, such as peak amplitude, waveform shape, and time series changes, when subjected to variations in material type, strip configuration, and impact velocity.

The following subsections present these comparison results sequentially by impact velocity. Within each velocity level, representative cases are selected for detailed discussion to highlight key differences or consistency trends. The complete dataset and additional results are provided in the Appendix.

4.2.1 Simplified setup correlation

To establish a basic correlation, results from a previous internal simulation of a simplified test configuration are shown in Figure 3.3, using the same assumed material properties listed in Table 3.1. Figure 4.4 below shows the correlation between the previously simulated pressure response and the measured test signal from earlier internal tests. Overall, the simulation captures the general pressure trend and approximates the peak magnitude, with slight differences in timing and unloading behavior. This initial correlation indicates that the basic tube model reasonably captures the main pressure response characteristics under simplified conditions. This provides a necessary baseline for extending the correlation to the advanced setup.

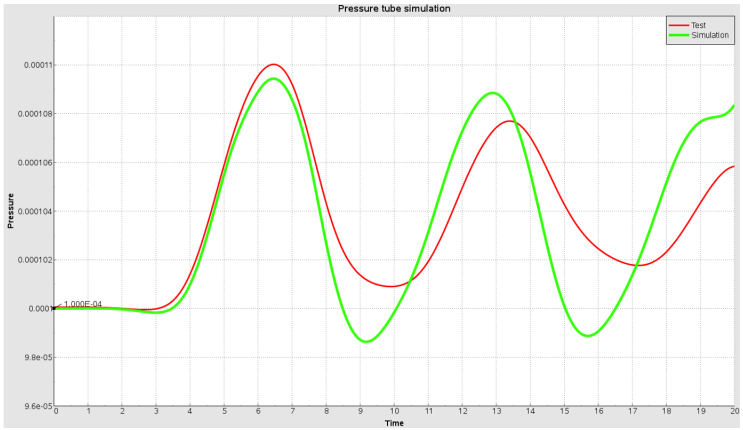

Figure 4.4: Pressure correlation: simplified configuration

4.2.2 Pressure response and correlation analysis at 2.5 m/s

To evaluate the pressure response under 2.5 m/s impact conditions with different constrained settings, the simulation results using Material 1 and Material 2 are compared against physical tests using tape and plastic straps. Figures 4.5 and 4.6 shows the pressure curves captured by both left and right sensors, respectively tested with 2 and 4 straps.

In each subfigure, the solid black and gray lines represent simulations with Material 1 and Material 2, while the dashed red and blue lines represent physical test results using tape and plastic straps. The time window for WIFac analysis is between 20–50 ms, which encompasses the rapid pressure rise, peak, and unloading phases.

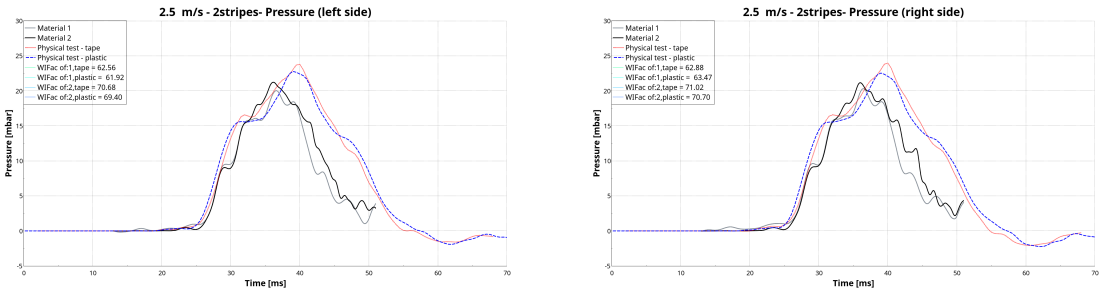

(a) Left sensor at 2.5m/s **(b)** Right sensor at 2.5m/s

Figure 4.5: Pressure curves at 2.5m/s with 2 straps

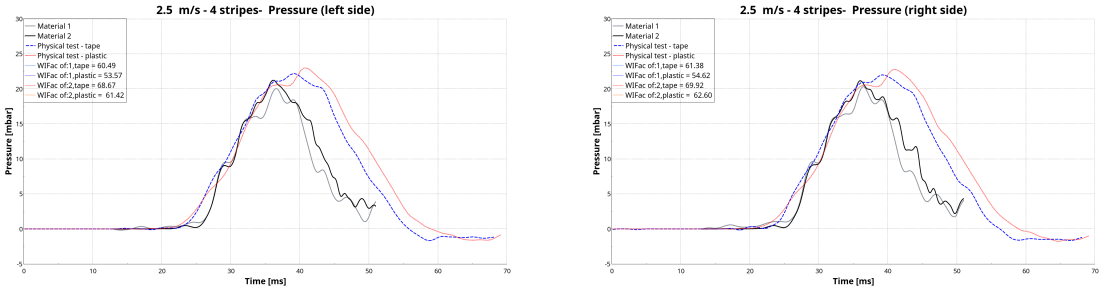

(a) Left sensor at 2.5m/s **(b)** Right sensor at 2.5m/s

Figure 4.6: Pressure curves at 2.5m/s with 4 straps

It can be observed that within the scope of the current test configurations, Material 2 achieves a higher correlation with the physical test results than Material 1. WIFac values for Material 2 exceed 70% on both left and right sensors in the 2-strap configuration. In the configuration with Material 1 and plastic straps, the WIFac values remain below 63%. For Material 2, WIFac values from the left and right sensors differ by less than 1%.

Regarding strap quantity, simulations with 2 straps consistently outperform those with 4 straps in terms of correlation. The use of 4 straps results in a wider spread between simulation and physical curves on both sides.

Table 4.4 also shows that simulation results using Material 2 is closer to the physical tests, it achieves a higher peak (21.23 mbar) than Material 1 (20.04 mbar). As shown in Table 4.4, pressure magnitudes are also underpredicted, with the simulation cases reaching their peaks earlier (36.1–36.5 ms) than the physical tests (39.0–42.0 ms).

Table 4.4: Comparison of maximum pressures at 2.5 m/s impact on the left side

Group	Type	Time(ms)	Max Pressure(mbar)
Reference	Material 1	36.5	20.04
	Material 2	**36.1**	**21.23**
Physical test A	2 tape straps	**39.0**	**22.78**
Physical test B	4 tape straps	41.0	22.20
Physical test C	2 plastic straps	**42.0**	**23.77**
Physical test D	4 plastic straps	41.5	22.99

As shown in Tables 4.5 to 4.8, Material 2 demonstrates superior performance compared with Material 1 in all configurations. WIFac values vary slightly between the left and right sensors. On the left side, Material 2 reaches values close to or above 70% in both the two-strap and four-strap setups, while Material 1 remains below 63%. On the right side, the difference between the two materials is similarly consistent, with Material 2 showing values approximately 7–15 percentage points higher than Material 1 depending on strap type. For both materials, the use of tape straps generally results in higher WIFac values than plastic straps.

Table 4.5: Correlation analysis for pressure curves at 2.5 m/s – 2 straps (left side)

Material	Speed (m/s)	Strap type	WIFac (%)
1	2.5	Plastic	61.92
1	2.5	Tape	62.56
2	2.5	Plastic	69.40
2	2.5	Tape	70.68

Table 4.6: Correlation analysis for pressure curves at 2.5 m/s – 4 straps (left side)

Material	Speed (m/s)	Strap type	WIFac (%)
1	2.5	Plastic	53.57
1	2.5	Tape	60.49
2	2.5	Plastic	61.42
2	2.5	Tape	68.67

Table 4.7: Correlation analysis for pressure curves at 2.5 m/s – 2 straps (right side)

Material	Speed (m/s)	Strap type	WIFac (%)
1	2.5	Plastic	63.47
1	2.5	Tape	62.88
2	2.5	Plastic	70.70
2	2.5	Tape	71.02

Table 4.8: Correlation analysis for pressure curves at 2.5 m/s – 4 straps (right side)

Material	Speed (m/s)	Strap type	WIFac (%)
1	2.5	Plastic	54.62
1	2.5	Tape	61.38
2	2.5	Plastic	62.60
2	2.5	Tape	69.92

4.2.3 Pressure response and correlation analysis at 3 m/s

The results now move on to the 3 m/s impact condition.

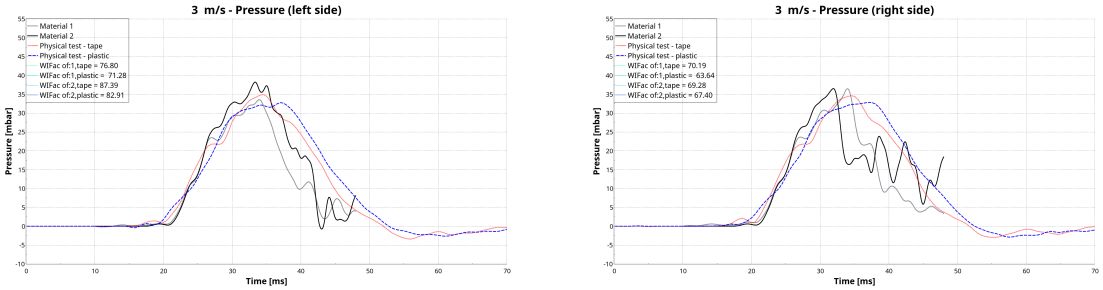

(a) Left sensor at 3 m/s **(b)** Right sensor at 3 m/s

Figure 4.7: Pressure curves at 3 m/s with 2 straps

As Figure 4.7 shows, the pressure curves of the left and right sensors display a clear rising phase, a distinct peak, and a subsequent unloading region. On the left sensor, Material 1 slightly underestimates the peak pressure and stays closer to the tape test curve, while Material 2 overestimates the peak and shows a steeper unloading trend. On the right sensor, both materials produce peak pressures slightly higher than the physical tests and reach the peaks 2–4 ms earlier; Material 1 shows a slightly higher peak than Material 2.
Tables 4.9 and 4.10 listed the peak pressure values and the corresponding timings. On the left side, Material 1 reaches 33.57 mbar, which is closer to the physical test peak of 34.94 mbar than Material 2's value of 38.65 mbar. On the right side, both materials produce peak pressures around 36.5 mbar, slightly higher than the physical test peak of 34.62 mbar.

Table 4.9: Comparison of maximum pressures at 3 m/s impact (Left side)

Group	Type	Time (ms)	Max Pressure (mbar)
Reference	Material 1	33.55	33.57
	Material 2	33.95	**38.65**
Test A	2 tape straps	34.50	34.94
Test B	2 plastic straps	37.00	32.79

Table 4.10: Comparison of maximum pressures at 3 m/s impact (Right side)

Group	Type	Time (ms)	Max Pressure (mbar)
Reference	Material 1	33.97	36.46
	Material 2	31.92	36.50
Test A	2 tape straps	34.50	34.62
Test B	2 plastic straps	37.00	32.85

The WIFac analysis shown in Tables 4.11 and 4.12 provides the correlation scores for both sides. On the left sensor, Material 2 achieves slightly higher WIFac values than Material 1 for both strap types. On the right sensor, the WIFac values of the two materials are close overall, with Material 1 slightly higher in the tape configuration and Material 2 slightly higher in the plastic configuration.

Table 4.11: Correlation analysis for pressure curves at 3 m/s – Left side

Material	Speed (m/s)	Strap type	WIFac (%)
1	3	Tape	76.80
1	3	Plastic	71.28
2	3	Tape	87.39
2	3	Plastic	82.91

Table 4.12: Correlation analysis for pressure curves at 3 m/s – Right side

Material	Speed (m/s)	Strap type	WIFac (%)
1	3	Tape	70.19
1	3	Plastic	63.64
2	3	Tape	69.28
2	3	Plastic	67.40

4.2.4 Pressure curves for 4m/s

The results continues with the 4 m/s impact condition, where the pressure curves shows sharper peaks and faster dynamics compared to lower speeds. As shown in Figure 4.8, pressure on both left and right sensors shows a rapid rise, a clear peak, followed by an unloading phase. On the left side, Material 1 reaches the highest peak but unloads more quickly, whereas Material 2 provides a better fit to the overall physical curve shape. On the right side, Material 2 captures the pressure level more accurately, though still with slight overprediction in some regions.

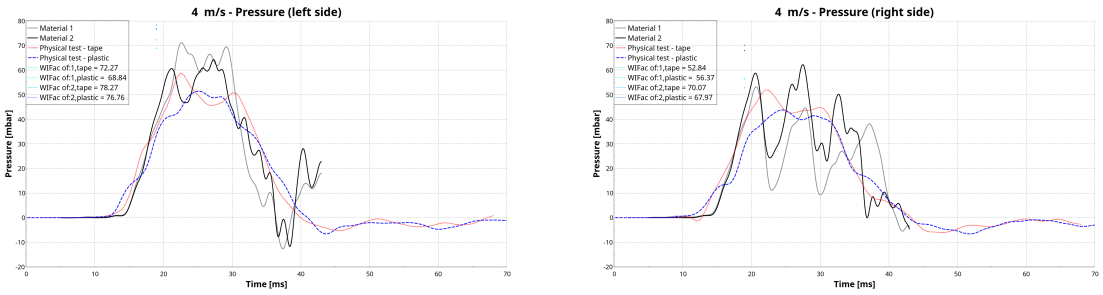

(a) Left sensor at 4m/s **(b)** Right sensor at 4m/s

Figure 4.8: Pressure curves at 4m/s with 2 straps

As shown in Tables 4.13 and 4.14, Material 1 reached a maximum pressure of 71.18 mbar at 22.63 ms on the left sensor, which is significantly higher than the physical peak. In contrast, Material 2 reached its peak at 64.26 mbar. Although this is still an overestimate, it is closer to the physical test value. On the right side, the peak of Material 2 (62.19 mbar) is also closer to the physical test value using tape (51.94 mbar), for Material 1 it occurs earlier. The simulated peaks appear 2–6 ms earlier than the corresponding physical test peaks.

Table 4.13: Comparison of maximum pressures at 4 m/s impact (Left side)

Group	Type	Time (ms)	Max Pressure (mbar)
Reference	Material 1	22.63	**71.18**
	Material 2	27.28	64.26
Test A	2 tape straps	24.50	58.85
Test B	2 plastic straps	25.00	**51.43**

Table 4.14: Comparison of maximum pressures at 4 m/s impact (Right side)

Group	Type	Time (ms)	Max Pressure (mbar)
Reference	Material 1	20.68	53.19
	Material 2	27.46	62.19
Test A	2 tape straps	24.00	51.94
Test B	2 plastic straps	24.50	**43.83**

As shown in Tables 4.15 and 4.16, Material 2 generally produced higher waveform correlation values (WIFac) than Material 1 across both sensor sides and strap types at 4m/s. On the left sensor, WIFac values for Material 2 were around 6 percentage points higher than those for Material 1 on the right sensor, the difference was more pronounced, with Material 2 exceeding Material 1 by over 10 percentage points in the tape strap configuration. In both cases, the use of tape straps resulted in slightly higher WIFac values than plastic straps for the same material.

Table 4.15: correlation analysis for pressure curves at 4 m/s – left side

material	speed (m/s)	strap type	WIFac (%)
1	4	tape	72.27
1	4	plastic	68.84
2	4	tape	78.27
2	4	plastic	76.76

Table 4.16: correlation analysis for pressure curves at 4 m/s – right side

material	speed (m/s)	strap type	WIFac (%)
1	4	tape	52.84
1	4	plastic	56.37
2	4	tape	70.07
2	4	plastic	67.97

4.3 Sensitivity analysis results

This chapter mainly focus on 3 m/s impact conditions to illustrate representative waveform trends, additional tests at 2.5 m/s and 4.0 m/s were also conducted.

The summary tables in Section 4.3.3 provide a comparative overview of all speeds. Complete tables and cases of secondary variation are included in the Appendix. Unless otherwise specified, the behavior of the left and right sensors is essentially consistent.

4.3.1 Displacement

For the factor impactor position, the sensitivity study was conducted that introduced a ±10 mm displacement along the longitudinal direction at 3 m/s. As Figure 4.9 shows, the baseline, +10 mm, and -10 mm curves initially follow the same trend.

As shown in Figure 4.9, at speeds of 3 m/s, when the impactor moves ±10–mm in displacement, the pressure response shows significant changes, particularly on the left side (Figure 4.9a). A backward displacement (–10 mm) results in a higher peak and better waveform alignment, while a forward displacement (+10 mm) reduces the peak and causes a slight delay. On the right side (Fig. 4.9b), the trend is similar but less pronounced.

This is reflected in the WIFac scores shown in the figure. The left side shows 89.7% for the −10 mm case and 83.4% for the +10 mm case. On the right side, WIFac drops more significantly from 85.7% to 75.1%.

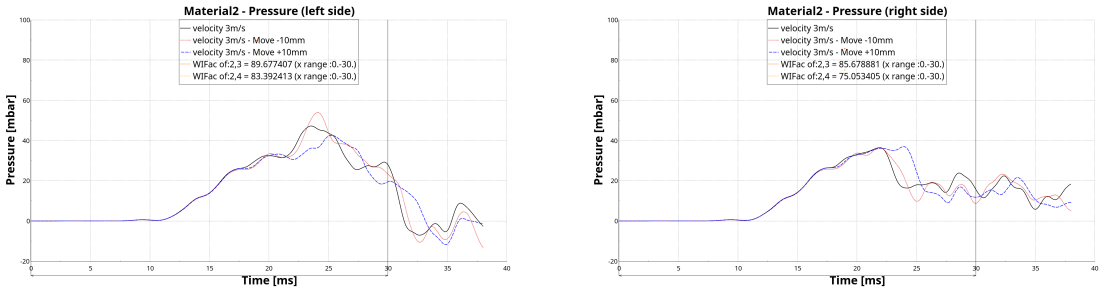

(a) Displacement – 3 m/s left **(b)** Displacement – 3 m/s right

Figure 4.9: Sensitivity analysis – 3 m/s displacement

4.3.2 Rotation

Regarding changes in rotation, with an impact velocity of 3 m/s, the impactor was rotated ±2° around the vertical axis. As shown in Figure 4.10, the small angular deviation in the initial setup moderately affects the pressure response.

On the left sensor (Figure 4.10a), both rotation directions result in peak pressures lower than the baseline,with a noticeable peak delay in the +2° case. The WIFac score decreased from 82.7% in the -2° case to 77.1% in the +2° case. Additionally, on the left side the pressure curve is overall closer to the physical test data than that on the right side.

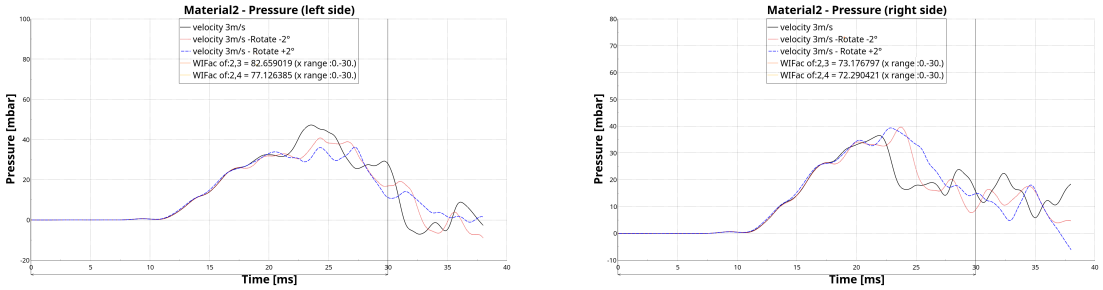

(a) Rotation – 3 m/s left **(b)** Rotation – 3 m/s right

Figure 4.10: Sensitivity analysis – 3 m/s rotation

4.3.3 Summary of Sensitivity Metrics

This subsection summarizes the changes observed in key metrics when varying rotation, initial position, and velocity at three different impact speeds: 2.5 m/s, 3.0 m/s, and 4.0 m/s. For each condition, the changes in maximum pressure, maximum acceleration (CFC1000), maximum deformation, and minimum post-impact velocity are compared to the original baseline case.

As shown in Table 4.17, at 2.5 m/s, all parameter changes result in only minor variations. Pressure and acceleration differ by no more than 2%, and deformation remains almost unchanged across all cases. This suggests low sensitivity at lower speeds, indicating good model stability in low-speed impacts.

At 3.0 m/s, as shown in Table 4.18, small variations produce more noticeable effects. The 10 mm backward displacement leads to a localized increase of 41% in peak pressure. The $-2°$ rotation results in a 7% rise in pressure and a 12% change in rebound velocity.

At 4.0 m/s, as shown in Table 4.19, the sensitivity remains observable. Rotational adjustments affect peak pressure by approximately 8–9%, while acceleration responses vary slightly, including small reductions.

Table 4.17: Summary of sensitivity metrics at 2.5 m/s (change compared to baseline)

Case	Max Pressure (%)	Max Acc. (%)	Max Deform. (%)	Min Velocity (%)
Rotate +2°	+1	+2	0	+0.3
Rotate -2°	+1	+2	-1	+0.1
Forward 10 mm	+0.1	+2	0	+0.2
Backward 10 mm	0	+1	0	+0.5

Table 4.18: Summary of sensitivity metrics at 3.0 m/s (change compared to baseline)

Case	Max Pressure (%)	Max Acc. (%)	Max Deform. (%)	Min Velocity (%)
Rotate -2°	+7	0	0	+12
Rotate +2°	-5	0	0	0
Forward 10 mm	+11	+1	0	0
Backward 10 mm	+41	+1	0	0

Table 4.19: Summary of sensitivity metrics at 4.0 m/s (change compared to baseline)

Case	Max Pressure (%)	Max Acc. (%)	Max Deform. (%)	Min Velocity (%)
Rotate -2°	+9	-1	0	0
Rotate +2°	+8	-2	0	0
Forward 10 mm	+7	+2	0	+1
Backward 10 mm	+10	-2	0	+1

4.3.4 Velocity

With velocity, all simulations behaved as expected. When adjusting the nominal speed of 3 m/s by ±2%, as shown in Figure 4.11, the response curves follow the expected trend: decreasing the speed reduces the pressure peak, while increasing it leads to a higher peak. This behavior is consistent on both left and right sensors.

On the left side (Figure 4.11a), the +2% velocity case produces the highest peak and an earlier pressure rise, while the −2% case shows a lower peak and delayed response. The WIFac values also support this trend, with 87.8% for +2% and 85.6% for −2%, both indicating strong shape similarity to the baseline.

On the right side (Figure 4.11b), the same trend is observed, though the pressure peaks are slightly less distinct. The corresponding WIFac scores are 81.3% (+2%) and 79.5% (−2%), suggesting a slightly lower correlation than on the left but still aligned with the expected pattern.

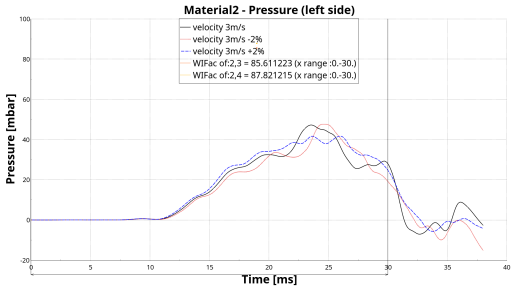

(a) Velocity – 3 m/s left

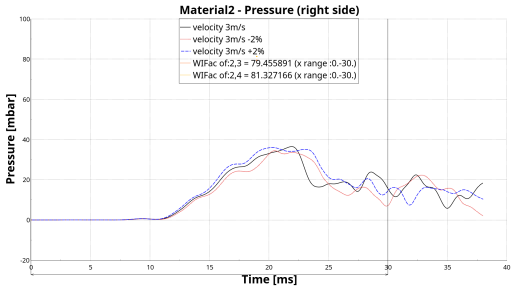

(b) Velocity – 3 m/s right

Figure 4.11: Sensitivity analysis – 3 m/s velocity change

4.4 PDI-2

In this section, the PDI-2 simulation results are compared against three physical tests conducted at the same nominal impact speed of 25 km/h. As shown in Figure 4.12, we noticed that each test produces a distinctly different response, the physical pressure signals exhibit substantial variability in both peak magnitude and waveform shape despite identical test conditions.

The purpose of including the PDI-2 comparison is not to correlate the advanced model, but to broaden the perspective. In future work, identifying which parameters most influence signal accuracy in high-fidelity models could help bridge the gap between simulated and real-world behavior.

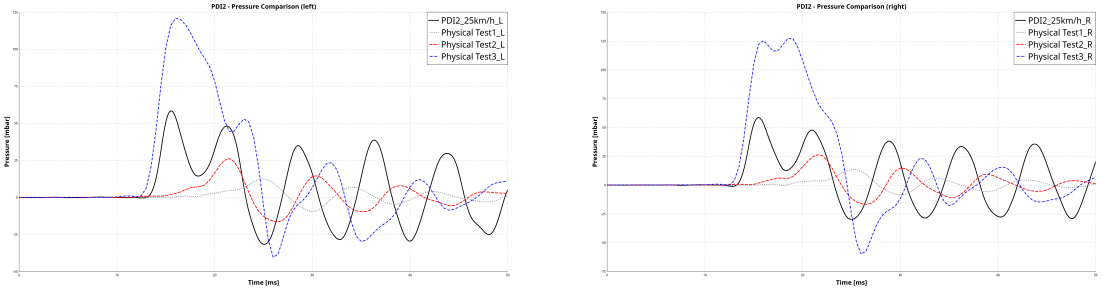

(a) PDI-2 test – left

(b) PDI-2 test – right

Figure 4.12: PDI-2 – test comparison

4.5 Young's modulus

To quantify the relationship between Young's modulus and the resulting peak internal pressure, a series of simulations were conducted at 3 m/s. The Young's modulus of the pressure tube was varied from 0.001 to 0.05 MPa to investigate its effect on the tube's mechanical response and the generated internal pressure. The resulting maximum pressure values are listed in Table 4.20.

Table 4.20: Effect of Young's Modulus on Maximum Pressure (3 m/s)

Young's Modulus (GPa)	Max Pressure (mbar)
0.001	35.5
0.0015	27.37
0.0016	25.57
0.0018	23.49
0.002	20.92
0.003	15.18
0.004	12.36
0.005	10.51
0.01	6.029
0.02	3.559
0.04	1.902
0.05	2.487

Figure 4.13 illustrates the relationship between Young's modulus and the maximum pressure response. The data clearly follow a nonlinear inverse trend, which can be approximated by a power-law function:

$$P = 0.186E^{-0.763} \tag{4.1}$$

This result aligns with the physical expectation that stiffer materials (higher E) deform less under impact, thus generating lower internal pressure peaks. Conversely, softer tubes (lower E) allow greater compression and produce stronger pressure signals.

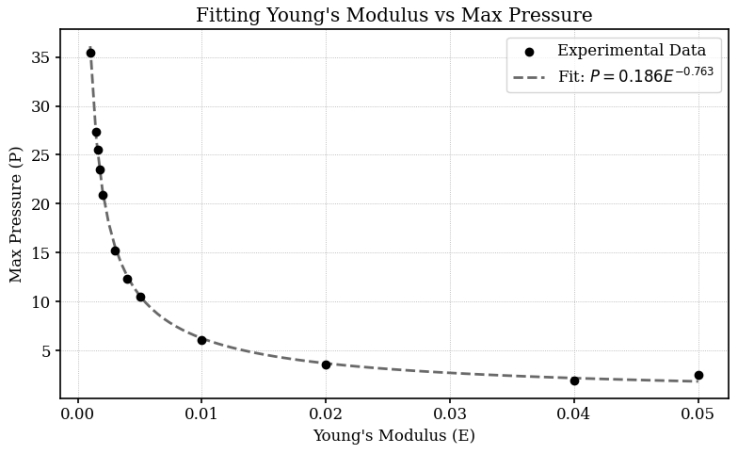

Figure 4.13: Fitting Young's Modulus vs Max Pressure at 3 m/s

The fitted curve illustrates the strong sensitivity of the simulated peak pressure to the assumed Young's modulus and highlights the need for accurate material property data in future model development.

5
Discussion

The aim of this thesis project is to evaluate the performance of a pressure tube sensor system using Finite Element (FE) simulation and to assess how well the simulation results correlate with physical impact tests, as well as to identify the factors influencing this correlation. Three research questions were posed to guide this work: (1) to identify factors influencing the simulation–test correlation, (2) to evaluate how well the signal outputs from simulation compare to physical dynamic tests, and (3) to evaluate the correlation between simulation results and physical test data from real-vehicle PDI-2 impact test.

The study first constructed a simplified model to familiarize itself with the ANSA, META, and LS-DYNA software tools. The simplified model reproduced the fundamental pressure trends and served as a baseline for the advanced system correlation. The model was refined by adjusting parameters such as material properties, and initial impact configuration. This resulted in a more advanced system model that integrated the complete bumper geometry and embedded foam structure to more realistically evaluate the system-level response under impact loads.

RQ1 - Evaluation of model limitations

Regarding RQ1, an analysis of the Young's modulus of the pressure tube reveals that it is the critical factor influencing simulation accuracy. The pressure response demonstrates a high degree of sensitivity to variations in this factor, exhibiting a nonlinear inverse relationship with peak pressure. This is because physically, a lower Young's modulus increases the wall compliance, leading to larger deformations under external impact loads. This greater deformation causes a more significant reduction in the tube's internal volume, which in turn raises the internal pressure. Moreover, the stiffness also affects the wave propagation speed and the interaction between the cross-sectional deformation and the enclosed air, both of which influence the peak pressure. A fitted power-law curve was established to describe this relationship, which may serve as a reference in future simulations. However, due to the lack of precise material data from the supplier and the unavailability of raw silicone rubber pieces for in-house testing at VCC, the modulus remains an assumed value. The second key factor is the foam material card. A comparison of the two available foam cards suggests that Material 2 performs better in replicating pressure amplitude and waveform shape, although further optimization is still required.

In addition, both ends of the pressure tube were defined as closed by setting BNDL

and BNDR to zero, replicating the intended sealing condition. The CAV parameter, which adjusts the end cross-section, was also kept at zero to prevent non-physical geometry changes, as attempts to modify it caused numerical divergence and were not further pursued. This reflects the physical setup: the pressure tube is not permanently sealed but is securely plugged into the sensor port, forming a tight connection robust enough that considerable force is required to disconnect it, which may help minimize the likelihood of air leakage under impact loading (see Figure 3.7).

RQ2 – Comparison between simulated and physical signals

Pressure

Regarding RQ2, the comparison between the advanced model simulations and physical tests suggests that the simulation generally captures the correct pressure response trends. The pressure curves typically reach their peak 3–6 ms earlier than the physical tests and begin unloading sooner, which can be attributed to the inherent characteristics of explicit time integration schemes. In explicit methods, the response is computed using small time steps without iterative equilibrium correction, which can cause the simulation to predict slightly faster wave propagation and unloading, especially in highly dynamic impacts. Here's the discussion in details about all these test configurations:

At an impact velocity of 2.5 m/s, waveform correlation assessed using WIFac analysis shows that Material 2 exhibits higher alignment with physical results than Material 1. In the 2-straps configuration, WIFac values for Material 2 exceed 70% on both left and right sensors (Tables 4.5, 4.7). In contrast, Material 1 combined with plastic straps yields lower correlation. Differences between the left and right sensors are minor (within 1%), suggesting sensor placement has limited influence under symmetric constraints at 2.5m/s. The comparison also suggests that tape straps consistently result in slightly higher WIFac values compared with plastic straps in all configurations at 2.5m/s. The combination of Material 2 and tape straps yields the highest correlation values (Table 4.5).

At 3.0 m/s, The WIFac analysis shown in Tables 4.11 and 4.12 illustrates that on the left side, Material 2 achieves notably higher correlation than Material 1, with an improvement of about 10 percentage points on average. For example, with tape straps, the maximum WIFac on the left reaches 87.4% for Material 2 compared to 76.8% for Material 1. On the right side, the overall difference between the two materials is smaller and depends on the strap type: Material 1 slightly outperforms Material 2 with tape straps, whereas Material 2 shows a marginally higher value with plastic straps.

At 4.0 m/s, WIFac analysis shows that Material 2 continues to outperform Material 1 in waveform correlation. The two tape straps configuration yields values of 78.27% and 70.07% on the left and right sensors, respectively (Tables 4.15, 4.16). Although some overprediction occurs, the overall shape of the pressure curve, particularly during the unloading phase, may be more consistent with the physical tests. Two

sensors differences are slightly larger than at lower speeds but still within 10%, suggesting limited influence of sensor position under symmetric constraints.

In summary, Material 2 generally exhibits higher waveform correlation than Material 1 across the tested impact velocities (2.5, 3.0, and 4.0 m/s). For most cases, the WIFac values of Material 2 in the two-tape-strap configuration are about 5–20 percentage points higher than those of Material 1. Despite slight overprediction at higher speeds, Material 2 maintains good consistency with the overall curve shape, particularly during the pressure unloading phase. Tape straps mostly produce higher WIFac values than plastic straps for both materials and sensor sides. Differences between left and right sensor results remain small at all speeds (within 1–10%), indicating that the placement of sensors does not significantly affect correlation quality under asymmetric boundary conditions. Overall, the combination of Material 2 and tape straps generally achieves the highest waveform correlation with the physical test results among the tested configurations, suggesting it is the most robust option for pressure simulation in this study.

Although Material 2 combined with tape straps yields the highest WIFac scores across all configurations, some deviations remain between simulation and physical test results. These deviations are not unexpected and a possible explanation could be as follows. First, the simulated pressure signals tend to reach peak values and begin unloading earlier than in the physical tests, which is a known characteristic of explicit time integration schemes used in LS-DYNA.

Second, slight differences between left and right sensor results are consistently observed. These may stem from the asymmetric foam constraints within the bumper, as shown in Figure 3.5. Uneven boundary conditions may lead to non-uniform local deformation, which propagates differently to each sensor.

Finally, at higher velocities, the foam undergoes stronger compression and rebound in the simulation, resulting in transient oscillations and small distortions in the predicted pressure signal. These oscillations are not prominent in the physical tests, a possible explanation might be that real materials and joints dissipate more energy through internal and interface damping than is represented in the current model. Despite this, the simulation still reproduces the key response trend, including the approximate peak magnitude and the rising phase, although differences remain in the unloading behavior and the presence of oscillations. This suggests that additional damping or improved contact definitions may be needed to better match the observed physical behavior at higher impact speeds.

While Material 2 shows a stronger correlation with the physical test results in most cases in this study, this does not imply that it should be directly used in full vehicle simulations without further validation. It is possible that the better agreement partly arises from compensating effects due to the simplified modeling of the foam restraints (tape and stripes). Therefore, dedicated material characterization and additional validation under different boundary conditions would be necessary before recommending Material 2 for system-level or full vehicle applications.

Kinematic response

Beyond local pressure signals, the overall kinematic response of the impactor was evaluated to further examine the consistency between simulation and physical test data. This included analysis of acceleration, velocity, and displacement from a reference node corresponding to the sensor location. Here's the discussion in details about all these kinematic response:

Acceleration comparisons showed that both materials consistently underestimated the peak values and predicted them earlier than in the physical test, which may indicate that the foam in the FE model is stiffer than the physical foam. However, the curve shape of Material 2 remained closer to the measured signal across all velocities. The WIFac values increased slightly with speed and remained above 68%, while Material 1 stayed below 63% (Table 4.1). These results align with the pressure response findings and suggest that Material 2 may better reflect the force transmission characteristics of the system.

For velocity, both materials showed high correlation at lower speeds. Material 2 achieved the highest consistency at 3.0 m/s, with a smoother deceleration trend over time. Material 1 exhibited a faster unloading slope, especially at 4.0 m/s, deviating from the physical test. This supports the observation that Material 2 better maintains temporal alignment in dynamic conditions (Table 4.2).

Displacement results revealed that both materials captured the deformation behavior well at 2.5 and 3.0 m/s, with WIFac values above 84%. At 4.0 m/s, however, Material 1's prediction dropped significantly, while Material 2 retained a closer match to the test curve (Table 4.3). This suggests that discrepancies in system-level deformation become more pronounced under higher impact conditions, further differentiating the two material models.

Taken together, the kinematic response analysis complements the pressure waveform findings. Material 2 appears to maintain higher consistency not only in localized pressure outputs but also in global dynamic behavior, particularly as the impact velocity increases.

Sensitivity

In addition to evaluating waveform consistency, sensitivity analysis was used to assess the robustness of the simulation setup. Small variations in initial conditions such as position, rotation, and velocity were introduced to reflect realistic uncertainties in test configurations. At 2.5 m/s, variations in input parameters had minimal effect on pressure, acceleration, deformation, and rebound velocity. At 3.0 m/s and 4.0 m/s, certain cases with a 10 mm backward displacement led to noticeable amplitude changes, particularly in peak pressure, as shown in Table 4.18, Table 4.19. However, waveform trends and WIFac values remained within a predictable range, indicating that the model preserves signal structure even under moderate variations.

Velocity variation tests as shown in Figure 4.11further support this stability. When adjusting the nominal 3 m/s impact speed by ±2%, the resulting pressure curves

showed predictable shifts in both peak magnitude and timing, consistent with physical expectations. This further validating the robustness of this system for input variation within regulatory tolerance ranges.The results showed that the overall system response remains stable under such perturbations.

In summary, the observed variability in pressure responses arises from several parameter-specific effects. The selected foam material card represents different approximations of the foam's compressive and hysteretic behavior, which in turn influences how impact energy is absorbed and dissipated during the collision. The silicone tube's Young's modulus directly affects the peak pressure magnitude and the timing of unloading. Different fixation methods (tape versus plastic straps) change how securely the foam stays in place, altering local contact conditions. Additionally, slight variations in impactor alignment introduce further fluctuations. Due to practical test limitations, these factors could not be fully controlled or repeated identically, resulting in the dispersion observed in physical test results.

It should be noted that while waveform consistency was quantified using WIFac in this thesis, more comprehensive validation frameworks such as ADVISER and CORA are also available. These methods combine multiple metrics—including peak values, timing, and curve shape—into a single weighted score, offering a broader assessment of model performance [32]. However, given the scope and computational constraints of this study, WIFac was selected as a practical and repeatable similarity metric, supported by its availability in META and straightforward implementation in Python for automated workflows. Future research may benefit from integrating WIFac with other complementary indicators or adopting multi-channel schemes to enhance overall validation reliability.

RQ3 - PDI-2 model comparison

For RQ3, the PDI-2 model was simulated and evaluated under real conditions. The analysis showed that more complex pressure tube models may lack sufficient universality when integrated into more complex biomechanical systems. For the advanced model constructed in this paper, more potential factors need to be considered when constructing more complex models, including changes in contact interactions, component stiffness mismatches, and multi-directional loads.

Overall, the CAE model developed in this thesis seems to capture the main response characteristics observed in the physical tests, including the approximate peak magnitude, the timing of the peak response (within a few milliseconds), and the general rising and unloading phases of the pressure signal, although some differences remain in the unloading slope and local oscillations. It exhibits sufficient sensitivity to material parameters, reasonable robustness to setting changes, and good correlation with experimental signals. For further study, further improvements are needed to fully support simulation-driven development of pressure tube safety systems. While the current model does not match the physical test results exactly, it provides a consistent reference for trend analysis. The differences suggest that the limited number of physical trials may not fully capture the system's inherent variability, and that boundary conditions, contact, or assumed material properties could also contribute

to discrepancies. Increasing the number of physical tests and improving the accuracy of material properties may help reduce this gap and better define a representative response range.

6
Conclusion

This chapter analyzes the simulation results of the advanced pressure tube FE model used in this thesis.

The model demonstrates reliable waveform correlation across all tested impact speeds, with the Material 2 and two tape straps configuration consistently achieving the highest WIFac values above 70%, which was the highest WIFac score among the different setups. This may serve as a useful basis for future developments.

The Young's modulus of the pressure tube appears to be the most critical parameter affecting simulation accuracy. A value of 0.001 GPa yielded the best match with test data in advanced test set up, and a strong nonlinear inverse relationship with peak pressure was identified. Although the modulus is currently an estimate, the established power-law trend offers a solid basis for future experimental validation.

The material card of the foam is also a critical factor in determining simulation accuracy. Material 2 generally exhibited higher waveform correlation at the tested speeds, suggesting that its material card may better approximate the overall dynamic response of the foam in this setup.

Finally, analysis of the full-leg impactor test results using the PDI-2 model indicates that significant deviations may still occur when testing more advanced models, even with the same configuration. This suggests that the current model requires further analysis and modification, as other factors may influence its repeatability. Boundary conditions, material properties, contact, and external factors may require more detailed analysis and consideration.

In summary, the developed FE model in this thesis achieved the highest waveform correlation under the conditions of Material 2 and two tape fixation configurations at three tested impact speeds. This result indicates that this combination is the most suitable configuration for the current test. Future research should focus on experimental verification of material properties and be extended to more complex whole-vehicle models with detailed contact and boundary conditions.

Bibliography

[1] World Health Organization. (2023). Global status report on road safety 2023: summary. Geneva: World Health Organization. Licence: CC BY-NC-SA 3.0 IGO.https://www.who.int/teams/social-determinants-of-health/safety-and-mobility/global-status-report-on-road-safety-2023

[2] International Transport Forum (ITF), *Road Safety Annual Report 2024*, OECD Publishing, Paris, 2024. Available at: https://www.itf-oecd.org/road-safety-annual-report-2024.

[3] Lee, T.-H., Yoon, G.-H., Kang, J.-W., & Choi, S.-B. (2017). An experimental comparison of the pedestrian safety performances of a spring actuator and a pyrotechnic actuator for deploying an active hood lift system. Proceedings of the Institution of Mechanical Engineers, Part D: Journal of Automobile Engineering, 231(7), 973–983. https://doi.org/10.1177/0954407017701534

[4] Ames, E., and Martin, P., Pop-Up Hood Pedestrian Protection, Paper Number 15-0111, 24th Enhanced Safety of Vehicles (ESV) Conference, 2015. Available at: https://www-nrd.nhtsa.dot.gov/departments/esv/24th/files/24ESV-000111.PDF.

[5] European Commission. (2025). Annual statistical report on road safety in the EU, 2025. European Road Safety Observatory. Brussels: Directorate General for Transport. https://road-safety.transport.ec.europa.eu/statistics-and-analysis/european-road-safety-data_en

[6] Bosch Mobility. (2024). Pressure tube sensor for pedestrian protection. Retrieved January 24, 2025, from https://www.bosch-mobility.com/en/solutions/sensors/pressure-tube-sensor/

[7] Feser, M., Klumpp, B., Krätschmer, M., et al., Pedestrian Protection Sensor Improves Frontal Crash Detection, *ATZ Elektronik Worldwide*, 9, 2014, pp. 20–25. Available at: https://doi.org/10.1365/s38314-014-0246-6.

[8] Solanki, K., Oglesby, D., Burton, C., Fang, H., et al., Crashworthiness Simulations Comparing PAM-CRASH and LS-DYNA, SAE Technical Paper 2004-01-1174, 2004. Available at: https://doi.org/10.4271/2004-01-1174.

[9] Stamatiadis, N., Gender effect on the accident patterns of elderly drivers, Journal of Applied Gerontology, 15(1), 1996, pp. 8–22. Available at: https://doi.org/10.1177/073346489601500.

[10] Lopez-Valdes, F. J., Mascareñas Brito, A., Agnew, A. M., Cripton, P., Kerrigan, J., Masouros, S., et al., The ethics, applications, and contributions of cadaver testing in injury prevention research, Traffic Injury Prevention, 25(8), 1115–1128, 2024. Available at: https://doi.org/10.1080/15389588.2024.2376937.

[11] Larsson, K.-J., Blennow, A., Iraeus, J., Pipkorn, B., and Lubbe, N., Rib Cortical Bone Fracture Risk as a Function of Age and Rib Strain: Updated Injury Prediction Using Finite Element Human Body Models, *Frontiers in Bioengineering and Biotechnology*, 9, 2021. Available at: https://doi.org/10.3389/fbioe.2021.677768.

[12] Wayne State University, Detroit MI. (n.d). viewed 28 January 2022: Body Bequest https://bodybequest.med.wayne.edu/

[13] Klug, C., Bützer, D., Iraeus, J., John, J., Keller, A., Kowalik, M., Leo, C., Levallois, I., Putra, I. P. A., Ressi, F., Schmitt, K.-U., Svensson, M., Trummler, L., Wijnen, W., & Linder, A. (2023). How much does the injury risk between average female and average male anthropometry differ? – A simulation study with open source tools for virtual crash safety assessments. *Accident Analysis & Prevention, 193*, 107328.https://doi.org/10.1016/j.aap.2023.107328

[14] Leo, C., Rizzi, M. C., Bos, N. M., Davidse, R. J., Linder, A., Tomasch, E., & Klug, C. (2021). Are there any significant differences in terms of age and sex in pedestrian and cyclist accidents? *Frontiers in Bioengineering and Biotechnology, 9*, 677952. https://doi.org/10.3389/fbioe.2021.677952

[15] Rorris, L., Kolokythas, Y., & Pavlidis, V. (2010). Development of New Tools for Crash and Safety Analysis. Performance driven LS-DYNA simulation with ANSA and META.

[16] Jagota, V., Sethi, A. P. S., & Kumar, K. (2013). Finite Element Method: An Overview. *Walailak Journal of Science and Technology*, 10(1), 1–8.

[17] Lalwala, M., Chawla, A., Thomas, P., & Mukherjee, S. (2020). Finite element reconstruction of real-world pedestrian accidents using THUMS pedestrian model. *International Journal of Crashworthiness*, 25(4), 360–375.

[18] BETA CAE Systems. (2025). ANSA Pre-Processor, Software Version R25.0.1. Thessaloniki, Greece. https://www.beta-cae.com/ansa.htm

[19] BETA CAE Systems. (2025). META Post-Processor, Software Version R25.0.1. Thessaloniki, Greece. https://www.beta-cae.com/meta.htm

[20] AZoM. Silicone Rubber – Properties and Applications. Available at: https://www.azom.com/properties.aspx?ArticleID=920 (Accessed June 7, 2025).

[21] Niu, W., Zhang, M., Fan, Y. (2013): Effects of Bone Young's Modulus on Finite Element Analysis in the Lateral Ankle. *Applied Bionics and Biomechanics*, Vol. 10, No. 3, 2013, pp. 135–143. https://doi.org/10.3233/ABB-130081

[22] Longhitano, D., Henary, B., Bhalla, K., Ivarsson, J., et al., Influence of Vehicle Body Type on Pedestrian Injury Distribution, SAE Technical Paper 2005-01-1876, 2005. Available at: https://doi.org/10.4271/2005-01-1876.

[23] Bosch Mobility. (2024). Pressure tube sensor for pedestrian protection. Retrieved May 28, 2025, from https://www.bosch-mobility.com/en/solutions/sensors/pressure-tube-sensor/

[24] Feser, M., Klumpp, B., Krätschmer, M., & Lindner, B. (2014). Pedestrian Protection Sensor Improves Frontal Crash Detection. *ATZ elektronik worldwide*, 9(03), 20–24.

[25] Euro NCAP, ASSESSMENT PROTOCOL – VULNERABLE ROAD USER PROTECTION, Version 1.1.4, 2023. Available at: https://www.euroncap.

com/media/79885/euro-ncap-assessment-protocol-vru-v114.pdf (Accessed March 8, 2024).

[26] Mertz, H. J. (2002). Injury Risk Assessments Based on Dummy Responses. In Nahum, A. M., & Melvin, J. W. (Eds.), Accidental Injury: Biomechanics and Prevention (pp. 113–143). Springer, New York, NY. https://doi.org/10.1007/978-0-387-21787-1_5

[27] J. Davidsson, "Means to Reduce Traffic Related Fatalities and Injuries," Lecture presentation, Chalmers University of Technology, Gothenburg, Sweden, Oct. 30, 2023. Available at: 1_TME202_Lecture_Presentation_Means_to_reduce_traffic_related_fatalities_and_injuries_2023-10-30.pdf.

[28] K. D. Kusano and H. C. Gabler, "Safety Benefits of Forward Collision Warning, Brake Assist, and Autonomous Braking Systems in Rear-End Collisions," *IEEE Transactions on Intelligent Transportation Systems*, vol. 13, no. 4, pp. 1546–1555, Dec. 2012. Available at: https://doi.org/10.1109/TITS.2012.2191542.

[29] Altran Concept Tech GmbH, Pedestrian Detection Impactor 2 (PDI-2), Technical Product Manual, 2016. Available at: http://www.eontechsys.com/uploads/soft/190227/PDI-2.pdf.

[30] OICA Task Force DPPS. (2017). Scope and Limitations of the PDI-2 (Per Task Number 14, TF-DPPS/4/03, November 3rd 2017). Retrieved June 22, 2025, from https://wiki.unece.org/download/attachments/54428253/DPPS-4-03e.pdf?api=v2.

[31] Pal, C., Okabe, T., Vimalathithan, K., Manoharan, J., et al., Vehicle's Front End Profile Influence on Pedestrian Sensing System Using In-House Developed PDI-2 and Child FE Models, SAE Technical Paper 2016-01-1510, 2016. Available at: https://doi.org/10.4271/2016-01-1510.

[32] Untaroiu, C. D., Shin, J., & Lu, Y.-C. (2013). Assessment of a dummy model in crash simulations using rating methods. *International Journal of Automotive Technology*, 14(3), 395–405. Available at: https://doi.org/10.1007/s12239-013-0043-x.

A

Appendix 1

Appendix Table A.1: Raw simulation metrics at 2.5 m/s

Case	Max Pressure (mbar)	Max Acc. (g, CFC1000)	Max Deform. (mm)	Min Velocity (m/s)
Rotate +2°	21.93	210.7	43.22	1.322
Rotate -2°	21.77	214.3	43.45	1.325
Forward 10 mm	21.77	215.1	43.41	1.324
Backward 10 mm	21.81	211.4	43.41	1.328
Original	21.80	210.2	43.44	1.321

Appendix Table A.2: Raw simulation metrics at 3.0 m/s

Case	Max Pressure (mbar, CFC180)	Max Acc. (g, CFC1000)	Max Deform. (mm)	Min Velocity (m/s)
Rotate -2°	40.78	261.4	48.67	1.794
Rotate +2°	36.19	261.4	48.47	1.598
Forward 10 mm	42.56	262.6	48.64	1.597
Backward 10 mm	53.95	263.3	48.64	1.591
Original	38.23	261.1	48.66	1.596

Appendix Table A.3: Raw simulation metrics at 4.0 m/s

Case	Max Pressure (mbar, CFC180)	Max Acc. (g, CFC1000)	Max Deform. (mm)	Min Velocity (m/s)
Rotate -2°	67.17	365.9	58.62	2.118
Rotate +2°	66.72	364.7	58.43	2.108
Forward 10 mm	66.28	380.1	58.56	2.130
Backward 10 mm	67.78	362.6	58.60	2.119
Original	61.78	371.2	58.63	2.108

Appendix Table A.4: Raw simulation metrics for velocity sensitivity (±2%)

Speed (m/s)	Max Pressure (mbar)	Max Acc. (g, CFC1000)	Max Deform. (mm)	Min Velocity (m/s)
2.45	20.74	208.6	42.88	1.295
2.55	23.46	215.7	43.96	1.351
2.94	47.60	256.5	48.05	1.563
3.06	41.66	267.2	49.28	1.627
3.92	62.50	364.2	57.86	2.073
4.08	69.20	375.5	59.38	2.151

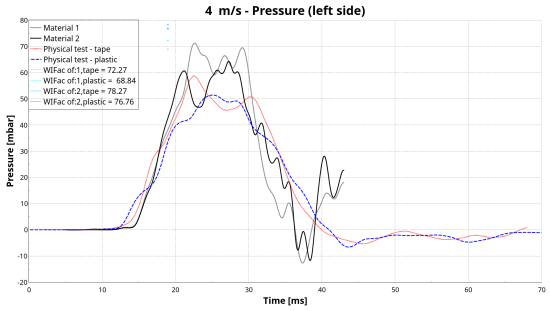

4 m/s Pressure (left side)

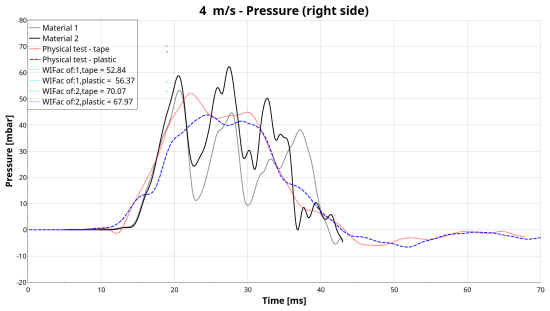

4 m/s Pressure (right side)

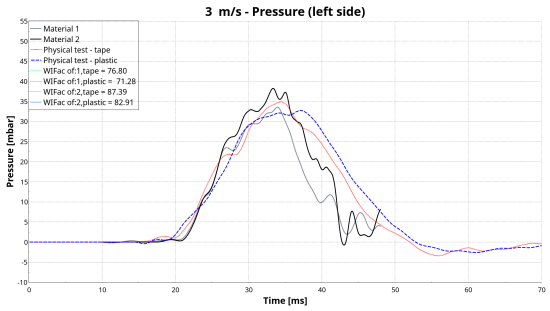

3 m/s Pressure (left side)

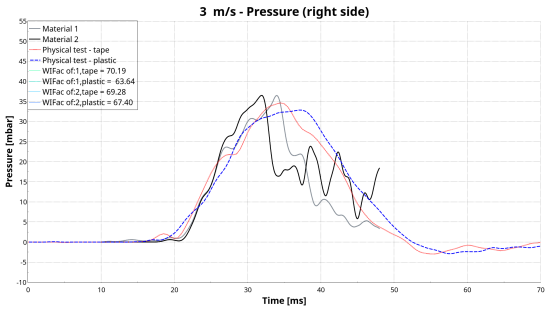

3 m/s Pressure (right side)

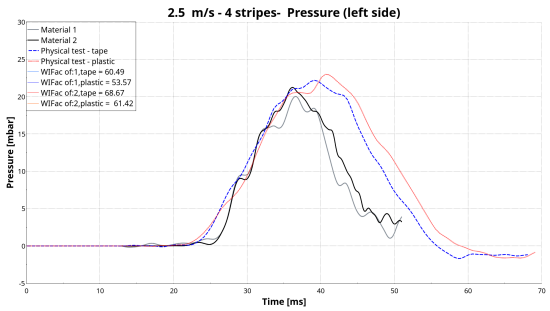

2.5 m/s Pressure (left side, 4 stripes)

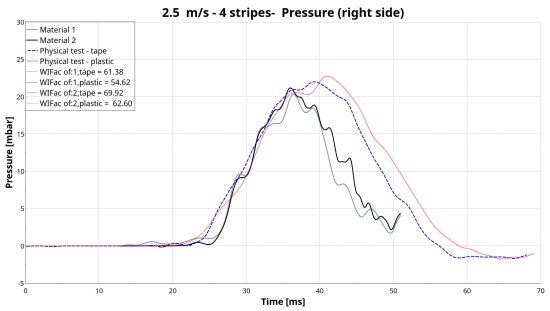

2.5 m/s Pressure (right side, 4 stripes)

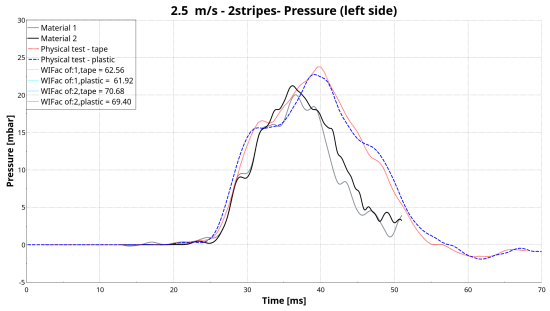

2.5 m/s Pressure (left side, 2 stripes)

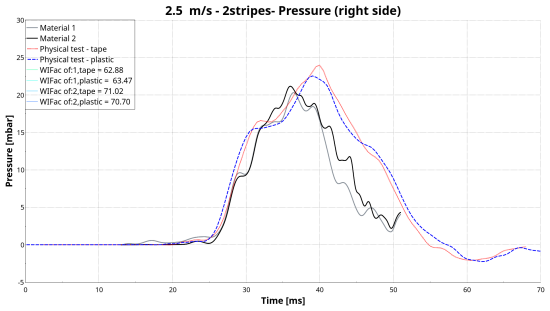

2.5 m/s Pressure (right side, 2 stripes)

Appendix Figure A.1: WIFac comparison of pressure curves for different materials and configurations

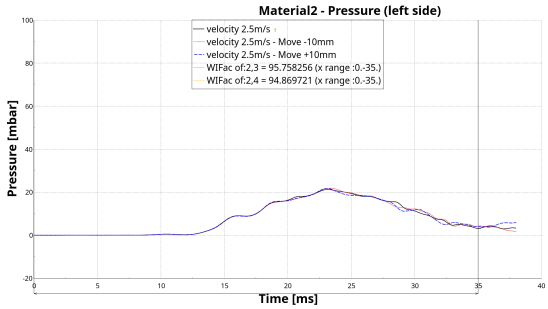

Move ±10 mm (left side)

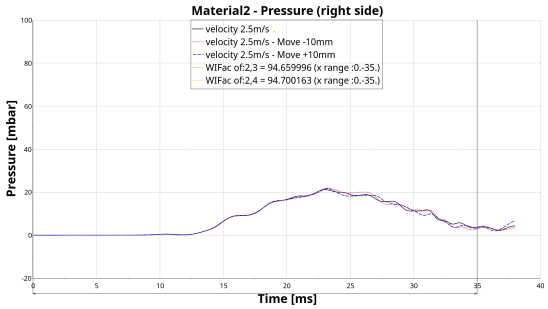

Move ±10 mm (right side)

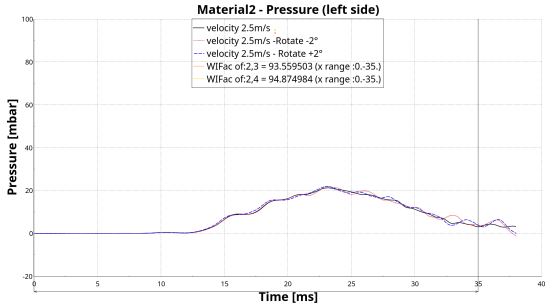

Rotate ±2° (left side)

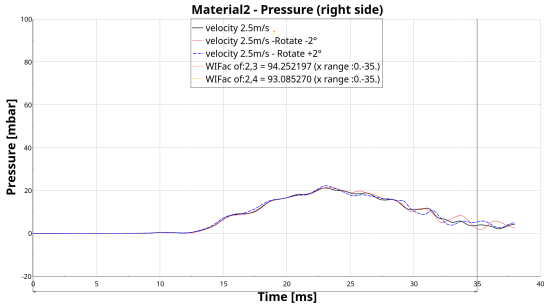

Rotate ±2° (right side)

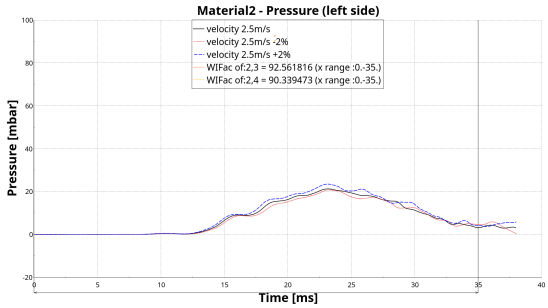

Velocity ±2% (left side)

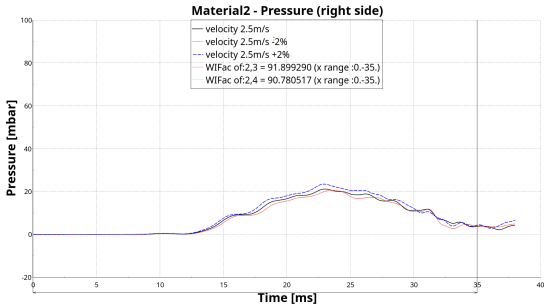

Velocity ±2% (right side)

Appendix Figure A.2: Sensitivity analysis of pressure curves at 2.5 m/s (Material 2)

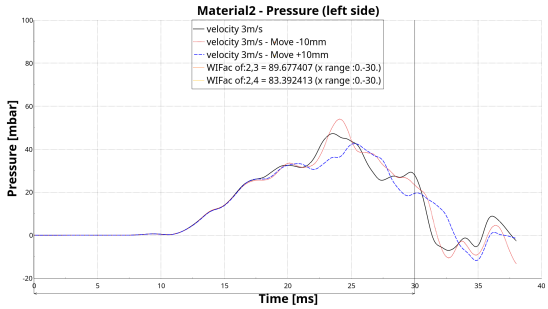

Move ±10 mm (left side)

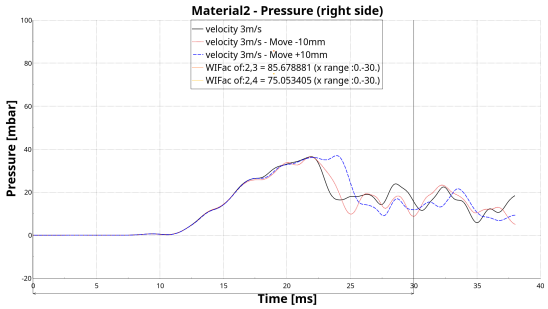

Move ±10 mm (right side)

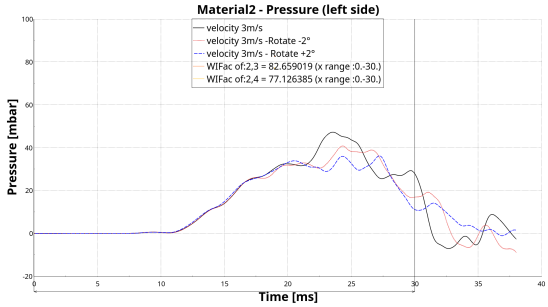

Rotate ±2° (left side)

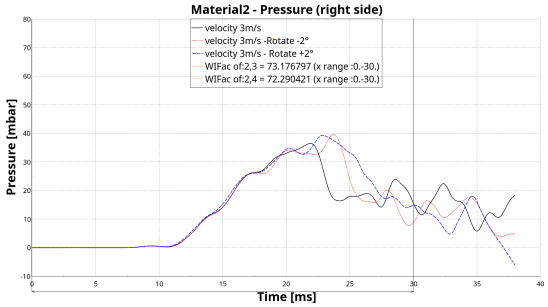

Rotate ±2° (right side)

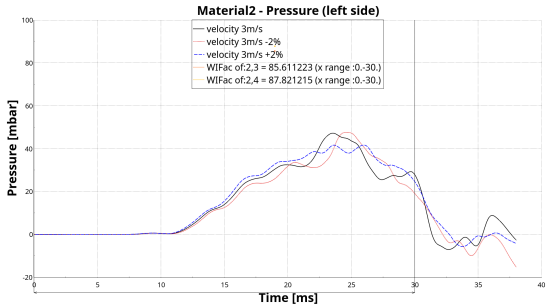

Velocity ±2% (left side)

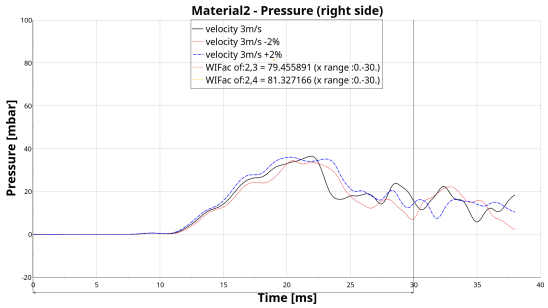

Velocity ±2% (right side)

Appendix Figure A.3: Sensitivity analysis of pressure curves at 3.0 m/s (Material 2)

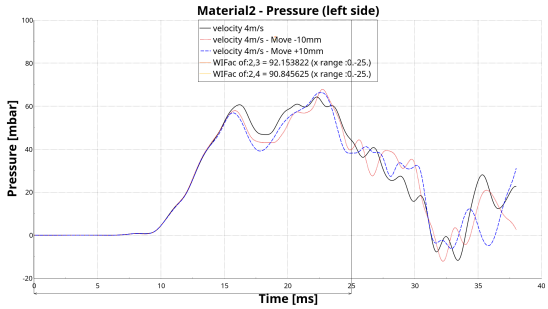

Move ±10 mm (left side)

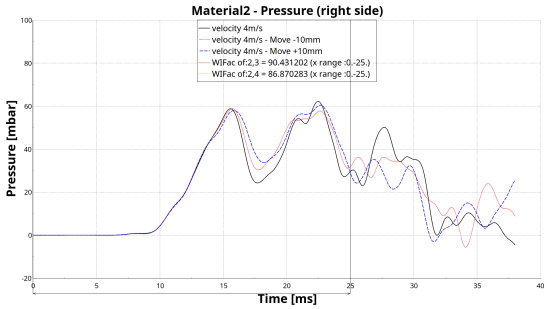

Move ±10 mm (right side)

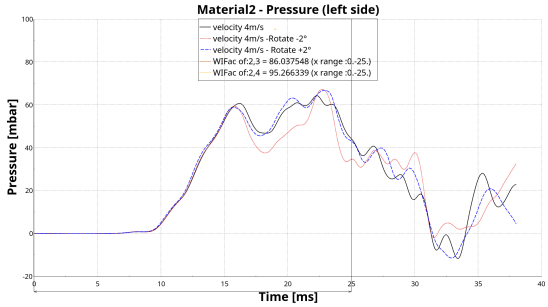

Rotate ±2° (left side)

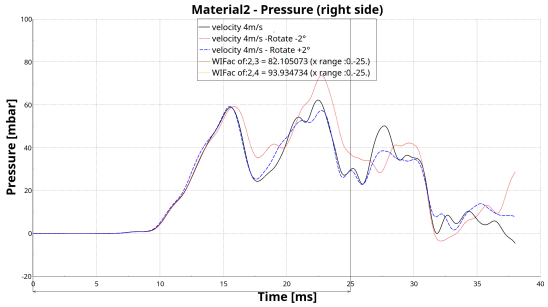

Rotate ±2° (right side)

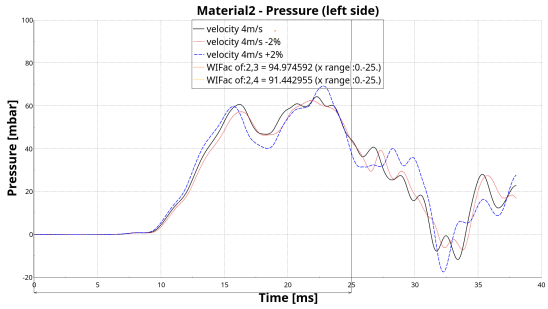

Velocity ±2% (left side)

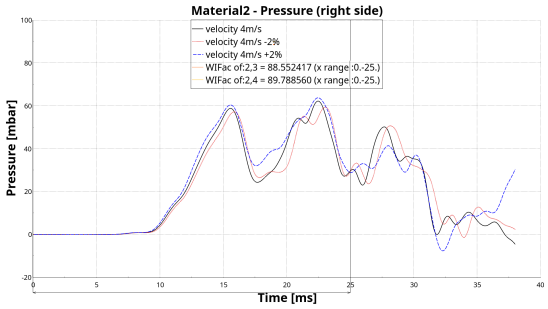

Velocity ±2% (right side)

Appendix Figure A.4: Sensitivity analysis of pressure curves at 4.0 m/s (Material 2)

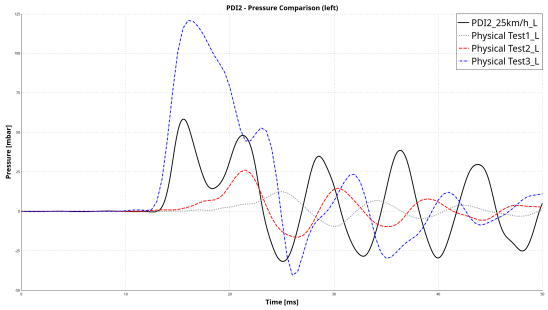

PDI2 vs Physical Test (left side)

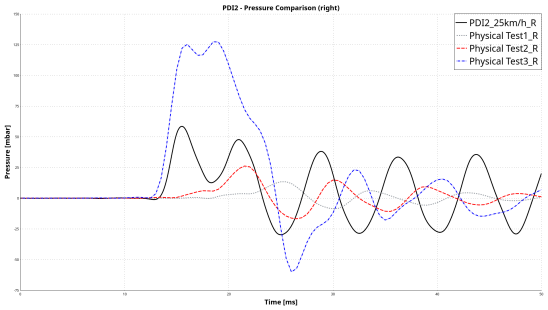

PDI2 vs Physical Test (right side)

Appendix Figure A.5: Comparison of simulated PDI2 results with three physical tests (Material 2, 25 km/h)

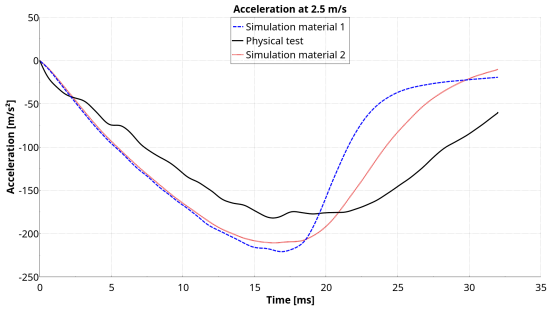

Acceleration at 2.5 m/s

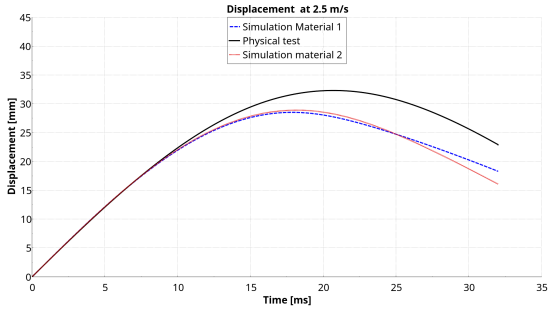

Displacement in Z at 2.5 m/s

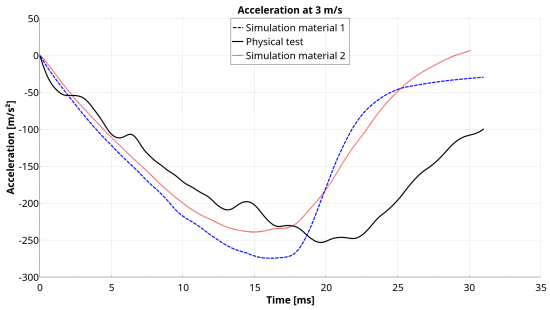

Acceleration at 3.0 m/s

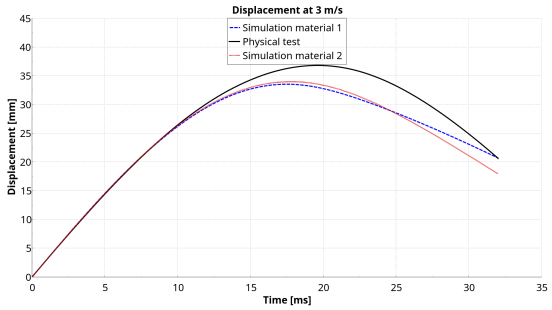

Displacement in Z at 3.0 m/s

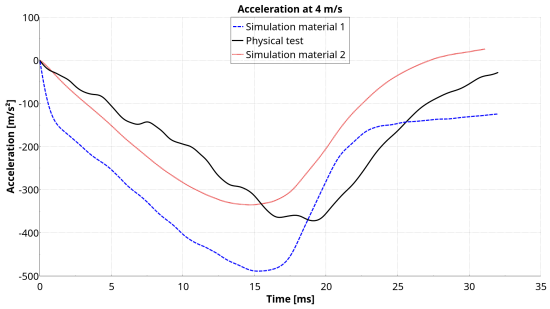

Acceleration at 4.0 m/s

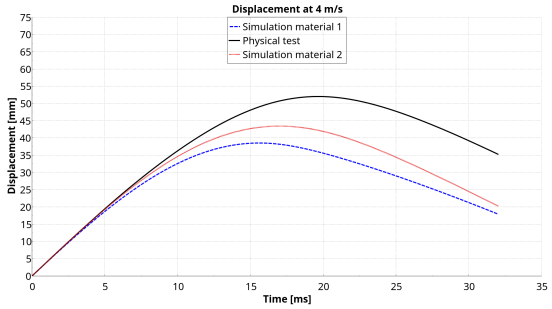

Displacement in Z at 4.0 m/s

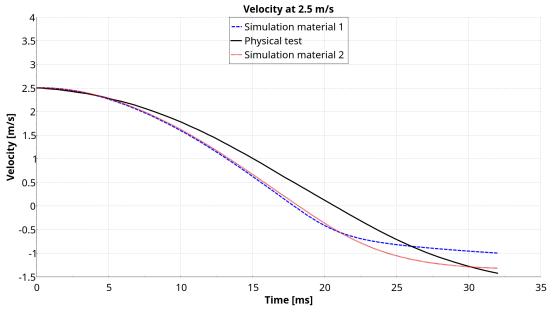

Velocity at 2.5 m/s

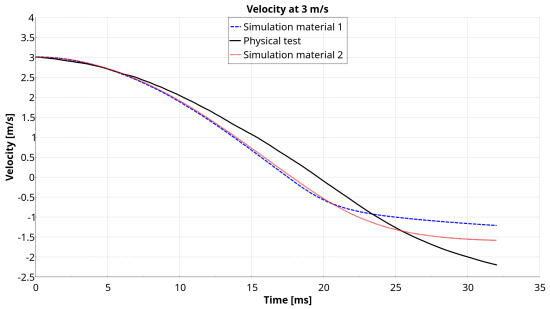

Velocity at 3.0 m/s

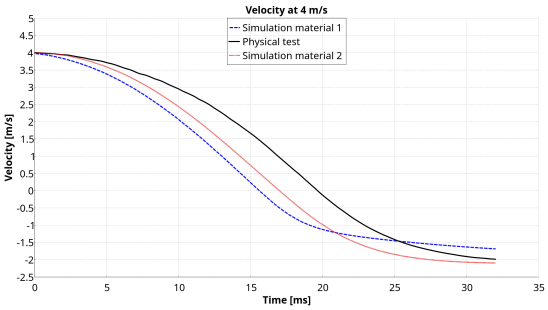

Velocity at 4.0 m/s

Appendix Figure A.7: Comparison of velocity curves at 2.5 m/s, 3.0 m/s, and 4.0 m/s

DEPARTMENT OF MECHANICS AND MARITIME SCIENCES
CHALMERS UNIVERSITY OF TECHNOLOGY
Gothenburg, Sweden 2025
www.chalmers.se

CHALMERS
UNIVERSITY OF TECHNOLOGY